Neuron

MAP2 Defines a Pre-axonal Filtering Zone to Regulate KIF1- versus KIF5-Dependent Cargo Transport in Sensory Neurons

Highlights

- MAP2 defines a unique pre-axonal cargo filtering zone in sensory neurons

- MAP2 regulates axonal cargo entry by preventing KIF5 binding to microtubules

- MAP2 promotes axonal cargo spreading by balancing KIF1 and KIF5 motor activities

- MAP2 controls the axonal growth potential of sensory neurons

Authors

Laura F. Gumy, Eugene A. Katrukha, Ilya Grigoriev, Dick Jaarsma, Lukas C. Kapitein, Anna Akhmanova, Casper C. Hoogenraad

Correspondence

c.hoogenraad@uu.nl

In Brief

Gumy et al. demonstrate that MAP2 defines a unique pre-axonal cargo filtering zone in sensory neurons that coordinates the activity of distinct kinesin motor proteins to drive selective cargo sorting and distribution in axons.

CellPress

Article

MAP2 Defines a Pre-axonal Filtering Zone to Regulate KIF1- versus KIF5-Dependent Cargo Transport in Sensory Neurons

Laura F. Gumy,[1,3] Eugene A. Katrukha,[1] Ilya Grigoriev,[1] Dick Jaarsma,[2] Lukas C. Kapitein,[1] Anna Akhmanova,[1] and Casper C. Hoogenraad[1,4,*]
[1]Cell Biology, Department of Biology, Faculty of Science, Utrecht University, 3584 CH Utrecht, the Netherlands
[2]Department of Neuroscience, Erasmus Medical Center, 3015 CE Rotterdam, the Netherlands
[3]Present address: Department of Anatomy, School of Biomedical Sciences, University of Otago, Dunedin 9054, New Zealand
[4]Lead Contact
*Correspondence: c.hoogenraad@uu.nl
http://dx.doi.org/10.1016/j.neuron.2017.03.046

SUMMARY

Polarized cargo transport is essential for neuronal function. However, the minimal basic components required for selective cargo sorting and distribution in neurons remain elusive. We found that in sensory neurons the axon initial segment is largely absent and that microtubule-associated protein 2 (MAP2) defines the cargo-filtering zone in the proximal axon. Here, MAP2 directs axonal cargo entry by coordinating the activities of molecular motors. We show that distinct kinesins differentially regulate cargo velocity: kinesin-3 drives fast axonal cargo trafficking, while kinesin-1 slows down axonal cargo transport. MAP2 inhibits "slow" kinesin-1 motor activity and allows kinesin-3 to drive robust cargo transport from the soma into the axon. In the distal axon, the inhibitory action of MAP2 decreases, leading to regained kinesin-1 activity and vesicle distribution. We propose that selective axonal cargo trafficking requires the MAP2-defined pre-axonal filtering zone and the ability of cargos to switch between distinct kinesin motor activities.

INTRODUCTION

Highly polarized cells like neurons require the accurate control of selective cargo trafficking pathways. However, how changes in individual vesicle motility properties translate into cargo distributions at the full-scale cellular level remains unknown. Recently, several local microtubule and kinesin-based mechanisms of axonal cargo transport in neurons have been elucidated, albeit their significance for global cargo distribution patterns is unclear (Song et al., 2009). Likewise, the dynamic compartmentalized movement of neuronal cargos has been described, although the precise mechanism underlying their distributions remains elusive (Wong et al., 2012). Thus, it is critical to determine the minimal basic mechanism required for the regulation of gross polarized axonal transport, from a molecular perspective.

Cytoskeleton-based motor proteins can drive selective axonal cargo transport in a regulated manner (Kapitein and Hoogenraad, 2011). Several regulatory mechanisms have been described that control the selective entry of cargos into the axon. Most studies have focused on the axon initial segment (AIS) as a specialized compartment in the proximal axon that plays a critical role in filtering intracellular trafficking (Leterrier and Dargent, 2014). In multipolar hippocampal neurons, vesicles containing somatodendritic cargos are selectively halted at the proximal axon, whereas cargos transporting axonal proteins are allowed to proceed through the AIS into more distal parts (Song et al., 2009).

Adult peripheral sensory neurons are widely used as model systems for the study of axonal regeneration and transport mechanisms (Maday et al., 2014). Yet, the molecular mechanisms underlying selective cargo transport and distribution in these neurons are completely unexplored. For instance, it is unknown why organelles such as lysosomes or most neuronal mRNAs are selectively retained in the cell body (Gumy et al., 2011), while adhesion molecules or secretory vesicles are actively transported into the axonal domain (Zhao et al., 2011). Defining how compartmentalized cargo movement is regulated in sensory neurons may thus provide a general mechanism for polarized cargo transport in neurons.

It has been speculated that microtubule-associated proteins (MAPs) might act as master regulators of axonal cargo transport. MAPs are strongly compartmentalized in neurons and could play an important role in regulating selective axonal cargo transport by controlling the activity of specific motor proteins (Atherton et al., 2013). However, little is known about the role of specific MAPs in regulating axonal cargo trafficking and their further impact on cargo distribution.

Classical MAPs are involved in many microtubule-related processes, such as microtubule assembly, stabilization, and cross-linking, and can interact with other cytoskeletal components or cellular proteins (Kapitein and Hoogenraad, 2015). MAP2 is structurally related to Tau, containing similar microtubule-binding regions but different projection domains that extend from the microtubule surface (Dehmelt and Halpain, 2005). MAP2 and Tau are very well known for their strict segregation into somatodendritic and axonal compartments, respectively. A set of in vitro studies have demonstrated that in the presence of
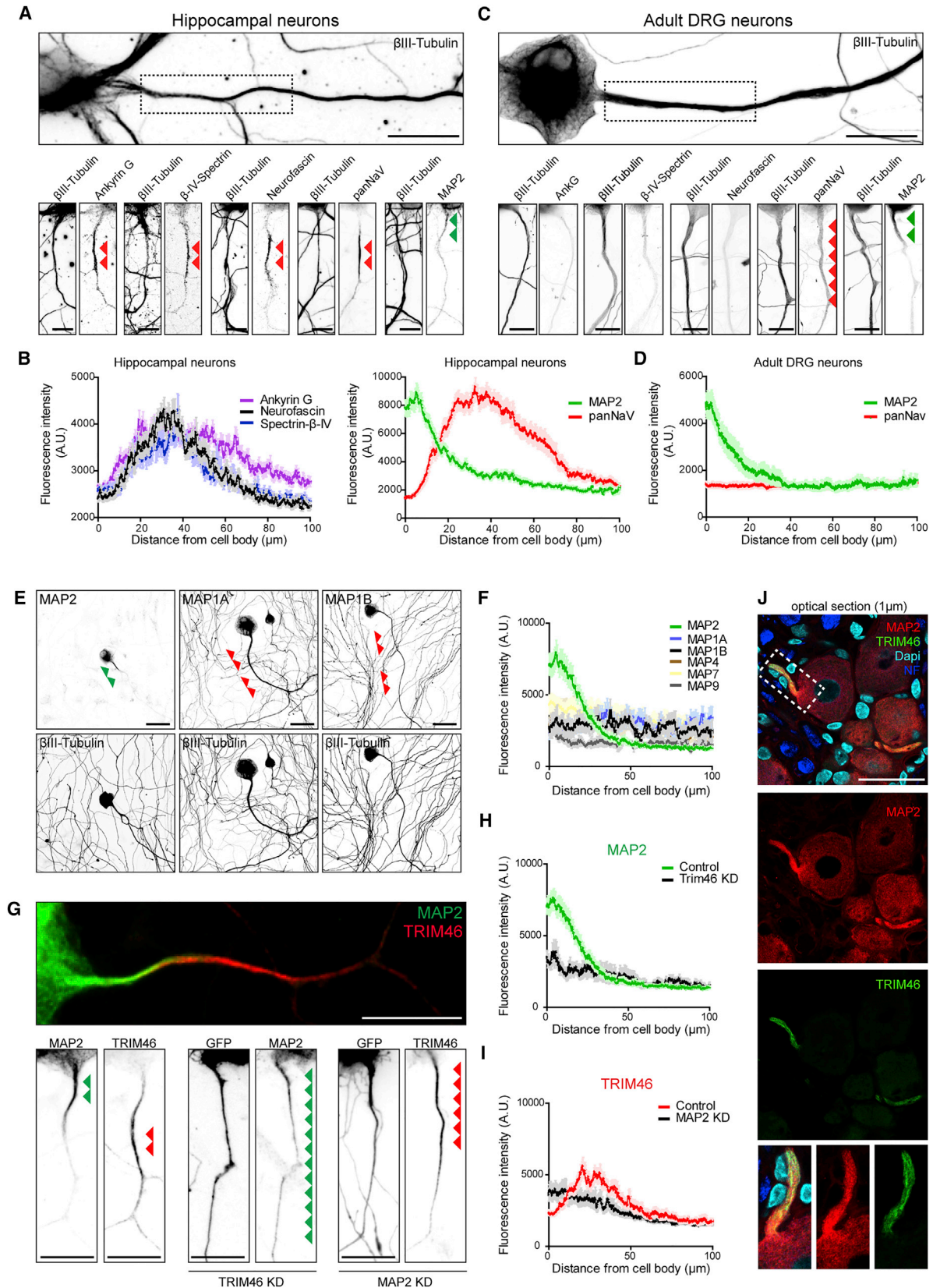
(legend on next page)

MAP2, kinesin-1 motility is inhibited (Hagiwara et al., 1994). However, it is currently unknown whether MAP2 regulates motor activity in neurons and, if so, what processes controls. Given the ubiquitous presence of MAP2 in many neuronal cell types, the ability of MAP2 to regulate motor activity makes it a likely candidate for providing local signals to control specific transport routes. So far, the role of MAP2 in regulating cargo trafficking has not been investigated. We have tested whether MAP2-dependent regulation of motor activity could underlie the basic principles of selective cargo sorting and distribution in neurons.

In this study, we used a combination of immunohistochemical, biochemical, cell biological, live-cell imaging, quantitative microscopy, and mathematical modeling approaches to determine the mechanisms underlying axonal cargo entry and transport in full-length sensory axons. We found that, despite the absence of a structured AIS, MAP2 specifically localizes to the soma and proximal axon of sensory neurons and defines a unique axonal cargo filtering zone. Here, MAP2 selectively retains lysosomes in the cell body, while promoting the axonal entry and distribution of secretory or dense core vesicles (DCVs). MAP2 promotes the axonal entry of secretory vesicles by regulating the cooperative action of "fast" kinesin-3 (KIF1) and "slow" kinesin-1 (KIF5) motors. In the proximal axon, non-microtubule-bound MAP2 inhibits slow kinesin-1 motor activity and allows fast kinesin-3 motors to drive robust DCV transport from the soma into the axon. In the distal axon where the inhibitory action of MAP2 dissipates, enhanced kinesin-1 activity results in the long-range distribution of DCVs along the axon. In this way, MAP2 controls the axonal entry and global distribution of cargos that contain distinct sets of kinesin motors. We propose a novel mechanism for selective axonal cargo entry and reveal a critical role for MAP2 as the gatekeeper of axonal cargo trafficking in sensory neurons.

RESULTS

MAP2 Specifically Localizes to the Soma and Proximal Axon in DRG Neurons

To gain more insight into the axonal cargo entry mechanisms in dorsal root ganglion (DRG) neurons, we first compared the localization of several AIS markers, including AnkyrinG (AnkG), βIV-spectrin, neurofascin (NF)-186, and voltage-gated sodium (Nav) channels in mature hippocampal and adult DRG neurons in culture. Consistent with previous studies (Hedstrom et al., 2008), all tested markers stained the proximal region of hippocampal axons outlining the AIS (Figures 1A and 1B). In addition, the microtubule-associated protein 2 (MAP2), a well-known somatodendritic marker in multipolar neurons, was also detected in the initial part of the proximal axon but did not overlap with the AIS (Figures 1A and 1B). In contrast, in DRG neurons, we were unable to detect marked enrichment of AnkG, NF-186, βIV-spectrin, or Nav channels in the proximal axon (Figures 1C and S1A). For instance, NaV channels were detected along the whole length of DRG axons (Figures 1C and 1D). Consistently, AnkG was enriched in the proximal axons of hippocampal neurons in juvenile and adult brains (Figure S1D) but was not detected in the proximal axon of DRG neurons in sections from rat and mouse whole DRGs (Figures S1E and S1F). In DRG sections, AnkG appeared largely enriched at the nodes of Ranvier (Figures S2E and S2F).

The MAP2B isoform (from here on referred to as MAP2) was abundantly expressed in mature hippocampal neurons and in adult DRG neurons (Figures S1B and S1C) and localized to the soma and initial part of the DRG axon in vitro and in vivo (Figures 1C, 1D, 1G, 1J, and S1E–S1G). At various days in culture, DRG neurons displayed different number of neurites that markedly changed over time before they formed one to two axons at 8 days in vitro (DIV8) (Figure S1H). MAP2 localized to the proximal part of every single neurite, regardless of the days in culture (Figure S1I). These findings are in line with a previous study where MAP2 was described to localize to the proximal axon during DRG neuron maturation in vitro (Hernández et al., 1989). To compare the specific staining pattern of MAP2 with other MAPs, cultured DRG neurons were immunostained for MAP1A, MAP1B, MAP4, MAP7, and MAP9. Quantitative analysis showed that most of the MAPs tested were equally distributed along the full axonal length, whereas MAP2 specifically localized to the proximal axon (Figures 1E, 1F, and S1J). The results demonstrate that adult DRG neurons in vitro and in vivo lack the enrichment of classic AIS markers but contain MAP2 in the initial part of proximal axon.

TRIM46-Dependent Localization of MAP2 in the Proximal Axon of DRG Neurons

We recently found that TRIM46 defines a specialized microtubule region in the proximal axon (van Beuningen et al., 2015). TRIM46 partly overlaps with MAP2 in the proximal axon of hippocampal neurons (Figure S1D). As in multipolar hippocampal neurons, TRIM46 specifically labeled the proximal axon of DRG neurons in vitro and in vivo (Figures 1G–1J and S1E). MAP2 and TRIM46 labeled partly overlapping compartments in cultured DRG neurons: MAP2 localized to the initial part of the proximal axon, whereas TRIM46 defined the more distal

---

Figure 1. MAP2 Localizes to the Proximal Axon of Adult DRG Neurons

(A and C) Hippocampal (A) or adult DRG neurons (C) (DIV7) immunostained with the indicated antibodies. Arrowheads indicate the specific staining.

(B and D) Average fluorescent intensity of MAP2 (hippocampal, n = 28; DRG, n = 29), panNav (hippocampal, n = 29; DRG, n = 30), Ankyrin G (n = 28), Neurofascin (n = 30), and β-IV-Spectrin (n = 18) in the proximal axon.

(E) Adult DRG neurons (DIV7) immunostained with the indicated antibodies. Green arrowheads; MAP2 staining. Red arrowheads; MAP1A or MAP1B staining.

(F) Average fluorescent intensity of MAP2 (n = 23), MAP1A (n = 17), MAP1B (n = 10), MAP4 (n = 10), MAP7 (n = 10), and MAP9 (n = 8) in the proximal axon.

(G) Immunostaining of MAP2 or TRIM46 in control, TRIM 46 knockdown, or MAP2 knockdown adult DRG neurons (DIV7).

(H and I) Average fluorescent intensity of MAP2 or TRIM46 in control (MAP2, n = 32; TRIM46, n = 30), TRIM46 knockdown (n = 15) (H), or MAP2 knockdown (n = 14) (I) adult DRG proximal axons.

(J) Immunohistochemistry of MAP2 and TRIM46 in adult DRGs in vivo.

A.U., arbitrary units. Mean ± SEM; at least three independent experiments. Scale bars indicate 25 μm (A), 100 μm (C and G), 200 μm (E), and 50 μm (J).
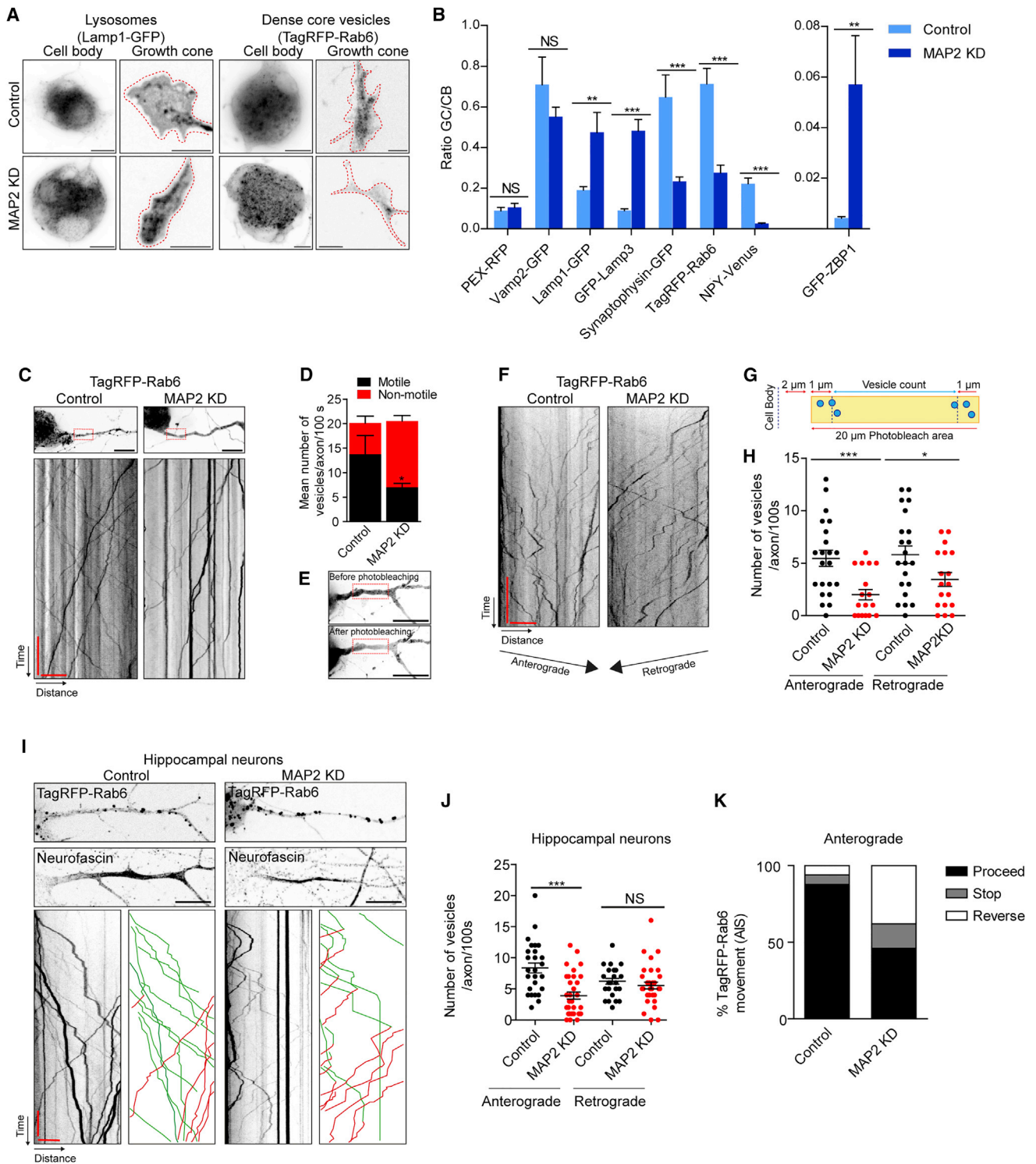
Figure 2. MAP2 Regulates the Axonal Entry of Dense Core Vesicles in Neurons

(A) Representative images of adult DRG cell bodies or growth cones (DIV4) cotransfected with the indicated constructs and an empty pSuper vector (control), or MAP2 shRNA (MAP2 knockdown). Traces highlight the growth cones.

(B) Ratio of fluorescence intensity of PEX-RFP (control, n = 20; MAP2 knockdown, n = 26), Vamp2-GFP (control, n = 29; MAP2 knockdown, n = 28), Lamp1-GFP (control, n = 29; MAP2 knockdown, n = 30), GFP-Lamp3 (control, n = 30; MAP2 knockdown, n = 29), Synaptophysin-GFP (control, n = 25; MAP2 knockdown,

part of the proximal axon in vitro (Figures 1G–1I). Immuno-stained sections of DRGs in vivo showed a very similar MAP2 and TRIM46 distribution pattern (Figures 1J, S1E, and S1F). Since TRIM46 regulates the compartmentalization of MAP2 in hippocampal neurons, we hypothesized that TRIM46 might also be involved in restricting the localization of MAP2 to the proximal axon in DRG neurons. Consistent with the data from hippocampal neurons, TRIM46 depletion caused the redistribution of MAP2 into the distal part of the axon, losing its characteristic proximal axon enrichment (Figures 1G and 1H). In contrast, MAP2 depletion caused a marked shift of TRIM46 toward the cell soma (Figures 1G and 1I). These results demonstrate that MAP2 localization in the proximal axon of DRG neurons depends on TRIM46.

MAP2 Controls the Axonal Growth Potential of DRG Neurons

To test the physiological function of MAP2 in adult DRG neurons, we knocked down MAP2, which caused a strong increase in the length of axons at DIV1 compared to controls (Figures S2A and S2B). To verify that the increase in axonal length was due to loss of MAP2 function, we cultured adult DRG neurons from MAP2 knockout (KO) mice and analyzed them at DIV1. Significantly, murine MAP2 KO DRG neurons also grew much longer axons compared to their wild-type counterparts (Figures S2C and S2D). The strong increase in axonal length was also observed in TRIM46-depleted DRG neurons where MAP2 is no longer enriched in the proximal axon (Figures S2E and S2F) and in MAP2-depleted hippocampal neurons (Figures S2G and S2H). Interestingly, MAP2 knockdown also affected the number of neurites per neuron. MAP2 depletion in adherent DRG neurons induced the outgrowth of new neurites from the cell body (Figure S2I). To establish the effects of MAP2 on neurite outgrowth, we depleted MAP2 in DRG neurons in suspension and subsequently plated these cells. Compared with the control, MAP2 depletion increased the percentage of neurons displaying multiple neu-rites, as well as in the overall mean neurite number (Figures S2J–S2L). In contrast, overexpression of MAP2 did not affect neurite outgrowth (Figure S2L). The efficiency of MAP2 knockdown or KO was confirmed by western blotting (Figure S2M). These results show that MAP2 localization to the proximal axon regulates the axonal growth potential of neurons.

MAP2 Regulates Cargo Filtering in the Proximal Axon of DRG Neurons

On the basis of both its marked enrichment in the proximal axon and its effect on kinesin-1 motor activity in vitro (Hagiwara et al., 1994), we hypothesized that MAP2 controls axonal cargo sorting and trafficking. Therefore, we expressed various specific organelle markers, such as peroxisomes (PEX-RFP), Vamp2-labeled membranes (Vamp2-GFP), lysosomes (Lamp1-GFP, GFP-Lamp3), RNA granules (GFP-ZBP1), synaptic vesicles (Synaptophysin-GFP), and secretory or dense core vesicles (DCVs) (TagRFP-Rab6, NPY-venus) and examined their distribution in the cell bodies and axonal growth cones of control and MAP2 knockdown neurons (Figures 2A and S3A). MAP2 depletion had no effect on the localization of peroxisomes and Vamp2-positive vesicles (Figure 2B). However, it strongly increased the axonal fraction of lysosomes and RNA granules and, in contrast, reduced the amount of synaptic vesicles and DCVs into the axon (Figure 2B). These data suggest that in DRG neurons MAP2 plays a role in specific cargo sorting by providing signals to retain vesicles in the cell body or by promoting cargo entry and distribution into the axon.

MAP2 Is Required for Proper Axonal Entry of Dense Core Vesicles

To further elucidate the role of MAP2 in selective axonal cargo entry, we focused on Rab6-positive secretory or dense core vesicles (DCVs). DCVs are generated in the cell body within the trans-Golgi network and are important for the delivery and rlease of neuopepties and other factors along axons and in the growth cones (Schlager et al., 2010). Also in DRG neurons, Rab6 colocalizes with the well-characterized DCV marker Neuropeptide Y (NPY) (Figures S3B–S3D). We depleted MAP2 and analyzed TagRFP-Rab6 transport in the proximal axon of DRG neurons. Live-cell imaging and kymograph analysis showed that the number of static and non-motile TagRFP-Rab6 vesicles increased in MAP2 knockdown neurons compared to controls (Figures 2C and 2D). To specifically visualize TagRFP-Rab6 vesicle dynamics in the initial part of the axon, the proximal axon was first photobleached and directly after imaged with fast acquisition (Figure 2E). Kymographs were used to quantify the number of entries of motile TagRFP-Rab6 vesicles into the photobleached area (Figures 2F and 2G). MAP2 depletion impaired the number

---

n = 26), TagRFP-Rab6 (control, n = 27; MAP2 knockdown, n = 31), NPY-Venus (control, n = 30; MAP2 knockdown, n = 28), and GFP-ZBP1 (control, n = 24; MAP2 knockdown, n = 23) in the growth cone (GC) versus cell body (CB) of control and MAP2 knockdown neurons.

(C) (Top) Still images from movies of adult DRG proximal axons (DIV4) cotransfected with TagRFP-Rab6 and an empty pSuper vector (control) or MAP2 shRNA (MAP2 knockdown). (Bottom) Kymographs of TagRFP-Rab6 vesicle motility in control and MAP2 knockdown adult DRG proximal axons.

(D) Number of motile and non-motile TagRFP-Rab6 vesicles in the proximal axon of control (n = 28) and MAP2 knockdown neurons (n = 29).

(E) Representative images of adult DRG proximal axons (DIV4) transfected with TagRFP-Rab6 before and after photobleaching.

(F) Kymographs of TagRFP-Rab6 vesicle behavior in the proximal axon of control and MAP2 knockdown DRG neurons (DIV4) after photobleaching.

(G) Schematic showing how TagRFP-Rab6 vesicle entries were counted after photobleaching the proximal axon.

(H) Number of control (n = 30) or MAP2 knockdown (n = 18) TagRFP-Rab6 vesicle entries in the proximal axon of adult DRG neurons (DIV4).

(I) (Top) Still images from movies of the AIS highlighted by Neurofascin live-staining of hippocampal neurons (DIV8) cotransfected with TagRFP-Rab6 and an empty pSuper vector (control) or MAP2 shRNA (MAP2 knockdown). (Bottom) Kymographs showing the behavior of TagRFP-Rab6 vesicles in the AIS of control and MAP2 knockdown hippocampal neurons.

(J) Number of axonal TagRFP-Rab6 vesicle entries in control (n = 27) and MAP2 knockdown (n = 34) hippocampal neurons (DIV8) after photobleaching.

(K) TagRFP-Rab6 vesicle dynamics in the AIS of hippocampal neurons (DIV8) (control, n = 226; MAP2 knockdown, n = 289).

Mean ± SEM. NS, non-significant; *p < 0.05; **p < 0.01; ***p < 0.001 (t test; at least three independent experiments). Scale bars indicate 10 μm (cell body panels) and 5 μm (growth cone panels) (A); (top) 100 μm, (bottom) 10 s and 5 μm (C); 20 μm (E); 10 s and 5 μm (F); (top) 10 μm, (bottom) 5 s and 5 μm (I).

of anterograde and, to a smaller degree, also retrograde moving Rab6 vesicles in the proximal axon (Figure 2H; Movie S1). Consistently, the number of anterograde NPY-venus and TagRFP-Rab6 entries from the soma into the axon was strongly reduced in MAP2 and TRIM46 knockdown DRG neurons, respectively, compared to the controls (Figures S3E–S3H). To assess a more general role of MAP2 in axonal cargo entry, we next analyzed TagRFP-Rab6 vesicle transport in hippocampal neurons after photobleaching. MAP2 knockdown significantly decreased the number of TagRFP-Rab6 axonal entries in hippocampal axons (Figures 2I and 2J). In control neurons, ~87% of Rab6 vesicles that entered the axon proceeded through the AIS, and ~6% reversed direction or paused (~6%) (Figure 2K). In MAP2 knockdown neurons, only ~46% of Rab6 vesicles proceeded through the AIS, while ~16% paused and ~38% of vesicles reversed direction (Figures 2K). Thus, also in hippocampal neurons, MAP2 in the proximal axon is required to allow the axonal entry of DCVs. We next tested whether the axonal transport phenotype was due to indirect changes in cytoskeletal organization. We observed a slight increase in the number of growing microtubule plus-ends and microtubule growth velocity in MAP2-depleted DRG neurons (Figures S4A–S4E), consistent with the role of MAP2 as a microtubule stabilizer (Dehmelt and Halpain, 2005). However, MAP2 depletion did not impair the orientation of plus-end out microtubules in DRG axons (Figure S4F), nor the organization of neurofilaments (Figures S4G and S4H). Furthermore, depletion of neurofilament L chain did not alter MAP2 localization in the proximal axon compared to controls (Figures S4I–S4K). These results suggest that MAP2 directly regulates DCV trafficking in the proximal axon of neurons.

Activity-Dependent MAP2 Phosphorylation Regulates the Axonal Entry of Dense Core Vesicles

Glutamate is the most abundant excitatory neurotransmitter in DRG neurons, plays an important role in the transmission of diverse stimuli, and is involved in nociceptive or neuropathic pain (Malet and Brumovsky, 2015). Previous studies showing that glutamatergic activity regulates the phosphorylation of MAP2 suggested that changes in its phosphorylation state might regulate diverse functions such as the transport of organelles or the interaction with microtubules (Quinlan and Halpain, 1996; Sánchez et al., 2000). We first determined whether glutamate stimulation affects overall MAP2 localization. We treated DRG neurons with 100 μM glutamate for 1 min, followed by extensive washout and fixation after 10 min. Quantification of total MAP2 distribution in the proximal axon showed no differences between control and glutamate-treated neurons (Figures 3A and 3B). We next examined the distribution of phosphorylated MAP2 (P-MAP2) after glutamate treatment. Addition of glutamate strongly decreased P-MAP2 signal in the proximal axon, in line with previous reports showing that glutamatergic treatment induces MAP2 dephosphorylation (Figures 3C and 3D) (Kapitein et al., 2011). To verify whether activity-dependent MAP2 dephosphorylation regulates DCV axonal entry, we analyzed the behavior of TagRFP-Rab6 vesicles in the proximal axon of control versus glutamate-treated and MAP2 knockdown glutamate-treated DRG neurons. Glutamate treatment

significantly increased the number of Rab6 axonal entries in both anterograde and retrograde directions, whereas MAP2 depletion prevented the glutamate-induced increase in trafficking (Figures 3E and 3F). These results demonstrate that MAP2 is required for mediating activity-dependent axonal DCV trafficking.

KIF1 and KIF5 Control the Axonal Entry of Dense Core Vesicles in DRG Axons

Previous reports have shown that kinesin-1 (KIF5) and kinesin-3 (KIF1) family members are involved in the transport of DCVs in hippocampal neurons (Schlager et al., 2010; Lo et al., 2011). To test whether these two kinesin family members are also required for DCV transport in DRG neurons, we examined the distribution of TagRFP-Rab6 in the cell body and axonal growth cone in KIF1- or KIF5-depleted neurons. Quantitative immuno-fluorescence was used to assess KIF1 knockdown efficiency in DRG neurons (Figures S4L and S4M). Similar to the MAP2 knockdown phenotype, simultaneous depletion of KIF1A/B/C strongly blocked DCV trafficking and led to vesicle accumulation in the cell body (Figures 4A and 4B). In contrast, when the KIF5B-tail region was used as a dominant negative to impair KIF5 activity (van Spronsen et al., 2013), Rab6 vesicles strongly accumulated at the growth cone, leaving the cell body depleted of vesicles (Figures 4A and 4B). The distal Rab6 vesicle accumulations were reversed by knockdown of KIF1 isoforms (Figures 4A and 4B), suggesting that KIF1 and KIF5 work together to drive DCV transport. We next determined the dynamic behavior of Rab6 vesicles in the proximal axon of KIF1- or KIF5-depleted neurons. Kymograph analysis showed that knockdown of KIF1 severely inhibited Rab6 vesicle movements (Figures 4C and 4D). KIF5 dominant-negative constructs led to strong accumulation of Rab6 vesicles in the growth cone with concomitant vesicle depletion from the cell body (Figures 4A and 4B). Under this condition, no Rab6 vesicle movement was observed in the proximal axon (Figure 4D). Together these results show that both KIF1 and KIF5 control DCV transport in adult DRG axons.

MAP2 Promotes Dense Core Vesicle Transport by Modulating KIF5 Motor Activity

To further investigate how these two kinesin motors cooperate to drive DCV transport, we turned to MRC5 human lung fibroblasts, which lack endogenous MAP2 (Figure 4E). We first measured the single-molecule speeds of KIF5B-MDC(1–560)-GFP (1.24 ± 0.20 μm/s) and KIF1C-MDC(1–397)-GFP (2.58 ± 0.68 μm/s) (motor domain and coiled-coil dimerization region, MDC; Lipka et al., 2016) (Figure 4F; Table S1A). These data show that distinct kinesin proteins have different velocities: KIF1 is a relatively fast motor and KIF5 a slow motor. In MRC5 control cells, Rab6 vesicles moved with a velocity of 1.60 ± 0.74 μm/s, which roughly falls between the single-molecule speeds of KIF5 and KIF1 (Figures 4F and 4G; Table S1A). Interestingly, expression of GFP-MAP2B in MRC5 cells strongly increased the velocity of Rab6 vesicles to 2.23 ± 1.07 μm/s (Figures 4E and 4G; Table S1A). These data are consistent with MAP2 as a promoting factor for DCV trafficking where it might modulate the activity of kinesin motors attached to Rab6 vesicles. To test this idea, we used
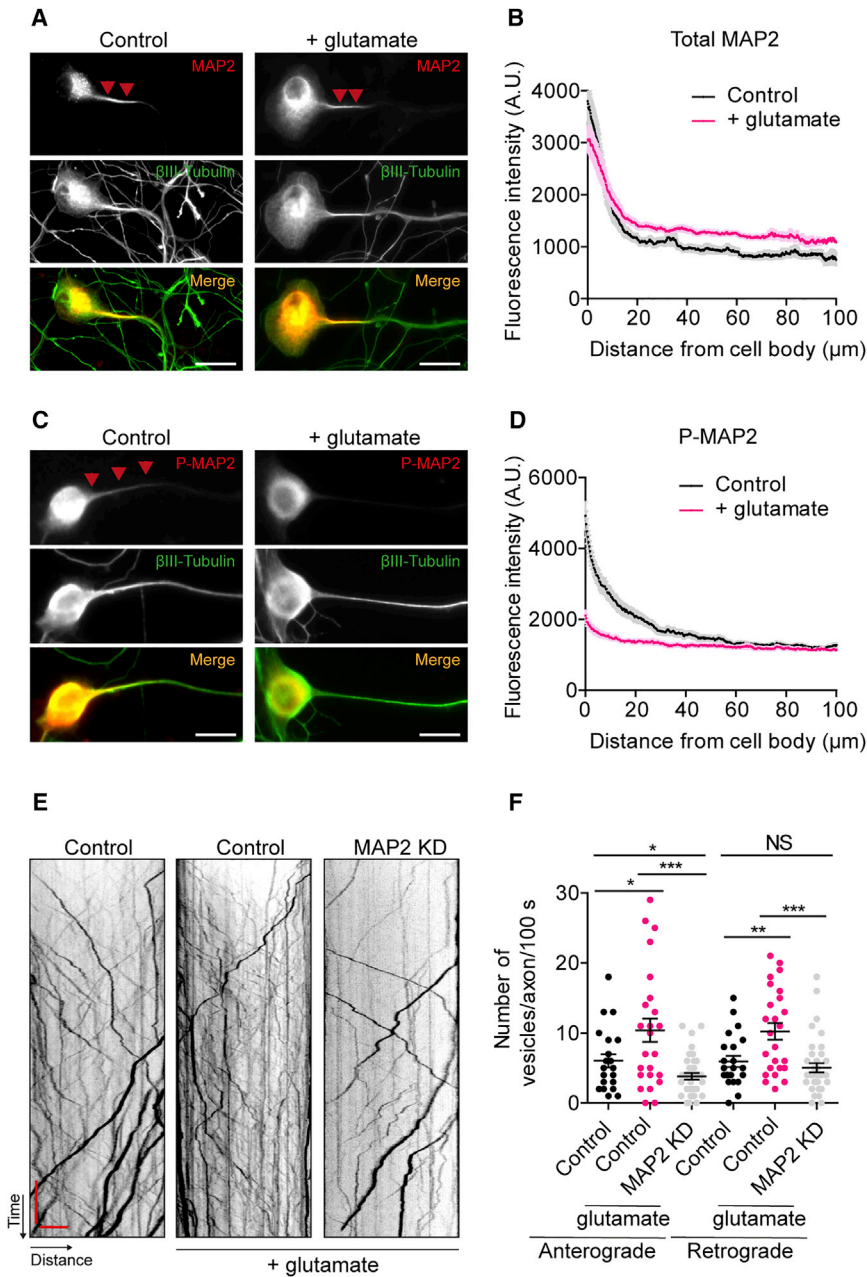
A Control / + glutamate (MAP2, βIII-Tubulin, Merge images)

B

Total MAP2

Fluorescence intensity (A.U.) vs Distance from cell body (μm)
— Control
— + glutamate

C Control / + glutamate (P-MAP2, βIII-Tubulin, Merge images)

D

P-MAP2

Fluorescence intensity (A.U.) vs Distance from cell body (μm)
— Control
— + glutamate

E Control / Control / MAP2 KD kymographs; + glutamate; Time vs Distance axes

F

Number of vesicles/axon/100 s

Control, Control, MAP2 KD (glutamate) — Anterograde; Control, Control, MAP2 KD (glutamate) — Retrograde

* ; *** ; NS ; * ; ** ; ***

Figure 3. Activity-Dependent Control of MAP2 Phosphorylation Regulates the Axonal Entry of Dense Core Vesicles in DRG Neurons

(A and C) Representative images of adult DRG neurons (DIV4) untreated (control) or treated with 100 μM glutamate (1 min) and immunolabeled with the indicated antibodies. Arrowheads, MAP2 staining.

(B and D) Fluorescent intensity of total MAP2 (B) or P-MAP2 (D) in the proximal axon of control (total MAP2, n = 19; P-MAP2, n = 27) and glutamate-treated (total MAP2, n = 29; P-MAP2, n = 28) adult DRG neurons.

(E) Kymographs showing TagRFP-Rab6 vesicle motility in the proximal axon of control, glutamate-treated, and MAP2 knockdown glutamate-treated adult DRG neurons (DIV4).
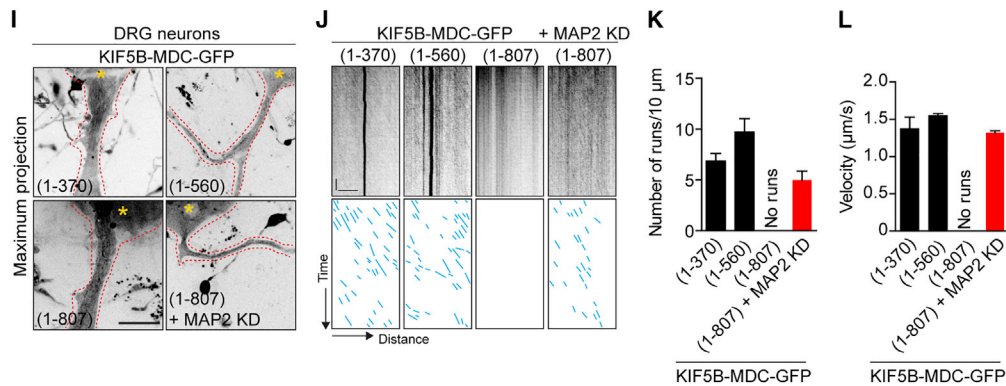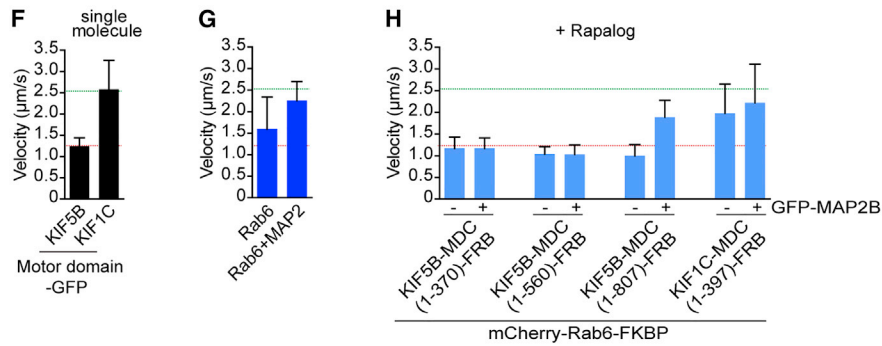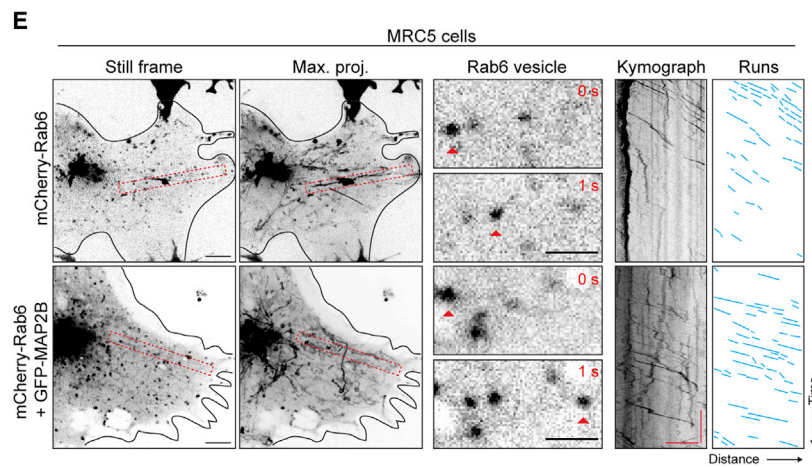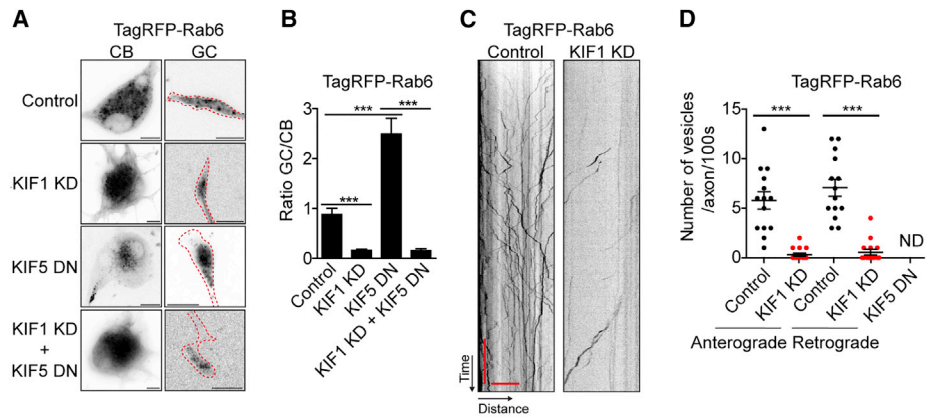
(F) Number of axonal TagRFP-Rab6 vesicle entries in control (n = 22), glutamate-treated (n = 25), and MAP2 knockdown glutamate-treated (n = 39) in adult DRG proximal axons after photobleaching.

Mean ± SEM. NS, non-significant; ***p < 0.001; **p < 0.01; *p < 0.1 (t test; at least three independent experiments). Scale bars indicate 10 μm (A and C) and 10 s and 5 μm (E).

the rapamycin FRB-FKBP inducible cargo trafficking assay, where we triggered the binding of KIF5B-MDC(1–807) or KIF1C-MDC(1–397) to Rab6 vesicles (Schlager et al., 2014). In line with previous reports (Schlager et al., 2014), recruitment of KIF1C-MDC(1–397) increased Rab6 vesicle velocity to 1.98 ± 0.67 μm/s (Figure 4H; Table S1A). However, expression of MAP2 had no effect on KIF1-driven motility. We next investigated whether MAP2 affected KIF5-driven cargo transport. Rab6 vesicles bound to KIF5B-MDC(1–807) moved with a relatively slow velocity of 1.0 ± 0.26 μm/s (Figure 4H; Table S1A). Strikingly, after addition of MAP2, the velocity of Rab6 vesicles increased to 1.89 ± 0.39 μm/s (Figure 4H; Table S1A). We interpreted this as an effect of MAP2 strongly blocking KIF5 motor

activity, allowing other fast endogenous motors, also attached to the vesicle and not affected by MAP2, to drive the vesicle's motility.

We next mapped which KIF5 region (amino acids 1–807) is implicated in this effect. To this end, we truncated the coiled-coil region in the KIF5B tail domain, KIF5B-MDC(1–560) and KIF5B-MDC(1–370). Interestingly, MAP2 did not affect the velocity of Rab6 vesicles attached to either of these two KIF5B truncations (Figure 4H; Table S1A), suggesting that the second coiled-coil region (560–807) in the KIF5B tail domain is required for MAP2-induced KIF5 motor activity inhibition on vesicles. In favor of an interplay between MAP2 and KIF5B-MDC(1–807), we observed that rapalog-induced binding of KIF5B-MDC(1–807) recruited cytoplasmic GFP-MAP2B to both stationary and motile Rab6 vesicles (Figure S5C; Movie S2). However, no MAP2 recruitment to Rab6 vesicles was observed before rapalog addition or using other KIF5B-MDC-GFP truncations. The association between MAP2 and Rab6 vesicles is further corroborated by findings showing that endogenous MAP2 colocalizes with Rab6 vesicles in the proximal axon of DRG neurons (Figures S5A and S5B). Furthermore, GFP-MAP2B was highly mobile throughout the cytoplasm, in contrast to isoform MAP2C, which strongly labeled microtubules (Figures S5D–S5F). Together these results show that kinesin-3 (KIF1) drives fast Rab6 vesicle trafficking and that kinesin-1 (KIF5) slows down Rab6 cargo transport.

A TagRFP-Rab6
CB   GC
Control
KIF1 KD
KIF5 DN
KIF1 KD + KIF5 DN

B TagRFP-Rab6
Ratio GC/CB
*** *** ***
Control, KIF1 KD, KIF5 DN, KIF1 KD + KIF5 DN

C TagRFP-Rab6
Control   KIF1 KD
Time
Distance

D TagRFP-Rab6
Number of vesicles /axon/100s
*** ***
Control   KIF1 KD   Control   KIF1 KD   KIF5 DN
Anterograde   Retrograde   ND

E MRC5 cells
Still frame | Max. proj. | Rab6 vesicle | Kymograph | Runs
mCherry-Rab6   0 s   1 s
mCherry-Rab6 + GFP-MAP2B   0 s   1 s
Time
Distance

F single molecule
Velocity (µm/s)
KIF5B   KIF1C
Motor domain -GFP

G Velocity (µm/s)
Rab6   Rab6+MAP2

H + Rapalog
Velocity (µm/s)
GFP-MAP2B − + − + − + − +
KIF5B-MDC (1-370)-FRB   KIF5B-MDC (1-560)-FRB   KIF5B-MDC (1-807)-FRB   KIF1C-MDC (1-397)-FRB
mCherry-Rab6-FKBP

I DRG neurons
KIF5B-MDC-GFP
Maximum projection
(1-370)   (1-560)
(1-807)   (1-807) + MAP2 KD

J KIF5B-MDC-GFP   + MAP2 KD
(1-370) (1-560) (1-807) (1-807)
Time
Distance

K Number of runs/10 µm
(1-370) (1-560) (1-807) (1-807) + MAP2 KD
No runs
KIF5B-MDC-GFP

L Velocity (µm/s)
(1-370) (1-560) (1-807) (1-807) + MAP2 KD
No runs
KIF5B-MDC-GFP

(legend on next page)

Moreover, MAP2 may promote Rab6 vesicle transport by inhibiting slow KIF5 motor activity, allowing KIF1 motors to drive fast transport.

MAP2 Impairs KIF5 Motor Activity in the Proximal Axon of DRG Neurons

To more directly examine the action of MAP2 on KIF5, we analyzed the single-molecule behavior of KIF5B-MDC-GFP truncations in proximal DRG axons. We found that both KIF5B-MDC(1–370)-GFP and KIF5B-MDC(1–560)-GFP displayed processive runs in control proximal axons, with mean velocities of 1.37 ± 0.16 μm/s and 1.55 ± 0.03, respectively (Figures 4I–4L; Table S1A). In contrast, KIF5B-MDC(1–807)-GFP did not show any processive motility in the proximal axon (Figures 4I–4L). Knockdown of endogenous MAP2 in axons rescued KIF5B-MDC(1–807)-GFP motility, which displayed processive runs (Figures 4I–4L; Table S1A), indicating that in DRG neurons MAP2 inhibits KIF5 motor activity.

MAP2 Inhibits KIF5 Motor Activity by Preventing the Binding of Kinesin to Microtubules

Motor inhibition can happen either by impairment of the motor's processive activity or by impeding the motor's association with microtubules. To determine the mechanism by which MAP2 inhibits KIF5 motor activity, we expressed TagRFP-MAP2B in MRC5 cells and compared the single-molecule performance of the KIF5B-MDC-GFP truncations with control cells (Figure 5A). Tracks were identified after performing maximum-intensity projections of KIF5 single-molecule runs imaged by TIRF live microscopy and were quantified by counting the number of KIF5 projected runs per 100 μm². Since KIF5 binds to microtubules and the maximum projection shows the total movement of KIF5 on microtubules over time, a decreased number of microtubule-like tracks correlates with less binding of KIF5 on microtubules. Quantification of the number of tracks from the maximum projection images showed that overexpression of MAP2 prevented the landing of KIF5B-MDC(1–807)-GFP on a large subset of microtubules (Figures 5A and 5B; Table S1B). However, in cells where the KIF5B-MDC-GFP truncations landed on microtubules, they engaged in processive runs, and MAP2 did not affect the single-molecule mean velocities compared to the controls (Figures S5G and S5H; Table S1B). To further study in detail

whether MAP2 prevents the binding of KIF5 to microtubules, we used the AMPPNP microtubule binding assay where the non-hydrolyzable ATP analog 5′-adenylylimididiphosphate (AMPPNP) locks kinesin motors in a microtubule-bound state (Hammond et al., 2010). After addition of AMPPNP, KIF5B-MDC(1–560)-GFP was efficiently bound to microtubules in both control (∼80%) and MAP2-expressing cells (∼80%) (Figures 5C and 5D). However, only ∼20% of MAP2-expressing cells had KIF5B-MDC(1–807)-GFP bound to microtubules compared to control (∼76%). Together our results suggest that MAP2 impairs KIF5 motor activity by affecting microtubule binding.

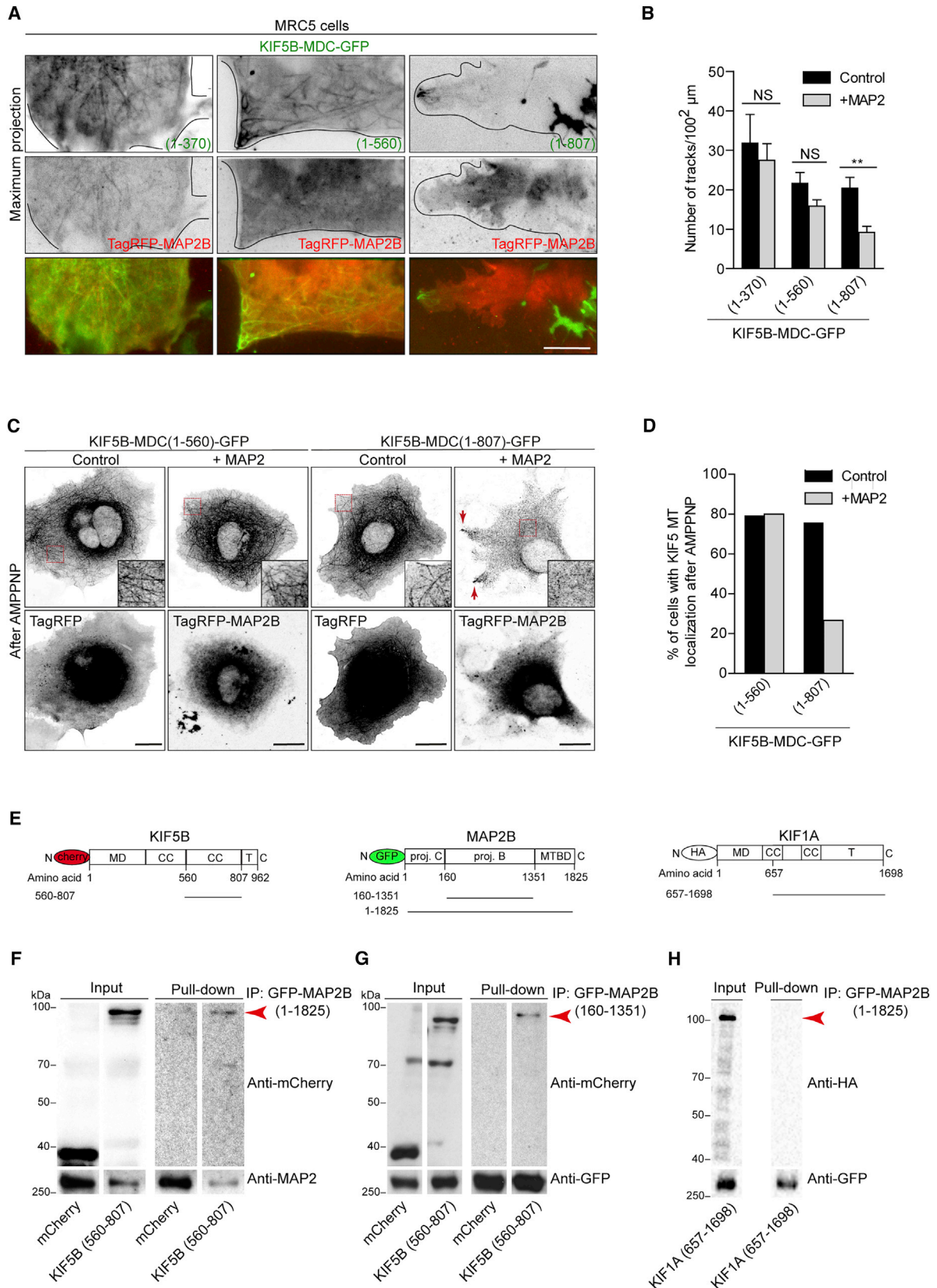### MAP2 Interacts with the Coiled-Coil Region of KIF5

To identify the domains of MAP2 and KIF5 involved in preventing the landing of the kinesin on microtubules, we set out to map the interaction sites of KIF5 and KIF1 with MAP2. We performed immunoprecipitation experiments with extracts of HEK293 cells expressing truncated versions of KIF5 or KIF1 and MAP2 (Figure 5E). Full-length GFP-MAP2B co-precipitated mCherry-KIF5B(560–807) (Figure 5F). KIF5(560–807) is the same region required for the effect of MAP2 in the cargo and single-molecule live-imaging experiments and in the AMPPNP microtubule binding assay (Figures 4E–4L and Figures 5A–5D). However, GFP-MAP2B did not co-precipitate HA-KIF1A(657–1698) (Figure 5H), indicating that MAP2 specifically interacts with KIF5. To further characterize the interaction site of MAP2 with KIF5, we created a truncated version of the projection domain of MAP2B. Truncated GFP-MAP2(160–1,351) co-precipitated mCherry-KIF5B(560–807) (Figure 5G), suggesting that the interaction between the projection domain of MAP2 and the coiled-coil region of KIF5 inhibits the binding of the kinesin to microtubules.

MAP2 Promotes the Spreading of Dense Core Vesicles into the Distal Axon

How does MAP2 inhibition of KIF5 regulate DCV vesicle distribution over long distances in DRG axons, as observed in Figure 2B? To answer this question, we imaged TagRFP-Rab6 vesicle motility from the soma to the growth cone (Figure 6A). Kymograph analysis of individual Rab6 vesicle tracks showed that in control axons the average number of anterogradely moving Rab6 vesicles decreased exponentially along the length of the

---

Figure 4. MAP2 Regulates Axonal Transport by Inhibiting KIF5 Motor Activity

(A) Representative images of adult DRG cell bodies (CB) or growth cones (GC) (DIV4) cotransfected with the indicated constructs. Traces highlight GCs.

(B) Ratio of fluorescence intensity of TagRFP-Rab6 in the GC versus CB (control, n = 28; KIF1 KD, n = 28; KIF5 DN, n = 21; KIF1 KD+KIF5 DN, n = 21).

(C) Kymographs illustrating TagRFP-Rab6 vesicle dynamics in the proximal axon of control or KIF1 knockdown adult DRG neurons (DIV4).

(D) Number of control (anterograde, n = 18; retrograde, n = 18), KIF1 knockdown (anterograde, n = 10; retrograde, n = 10) or KIF5 DN TagRFP-Rab6 vesicle entries in the proximal axon after photobleaching. ND, no data available as no moving vesicles were detected.

(E) Representative stills, maximum intensity projections, kymographs, and still zooms from mCherry-Rab6-FKBP time-lapse recordings of MRC5 cells cotransfected with an empty GFP vector or GFP-MAP2B. Arrowheads, moving vesicles.

(F) Mean velocity of KIF5B-MDC(1–560)-GFP or KIF1C-MDC(1–397) single molecules under the indicated conditions in MRC5 cells.

(G) Mean velocity of mCherry-Rab6-FKBP (Rab6) vesicles in the absence or presence of GFP-MAP2B (MAP2) in MRC5 cells.

(H) Mean velocity of mCherry-Rab6-FKBP under the indicated conditions in MRC5 cells.

(I and J) Maximum-intensity projections and kymographs of the indicated constructs in adult DRG proximal axons (DIV4) under control or MAP2 knockdown conditions. Yellow star, cell body.

(K and L) Mean number of runs (K) and velocity (L) of the indicated conditions in the proximal axon of adult DRG neurons (DIV4).

Mean ± SEM (B, D, K, and L). Mean ± SD (F–H). ***p < 0.001 (t test; three independent experiments). Scale bars indicate 10 μm (cell body panels) and 5 μm (growth cone panels) (A); 10 s and 10 μm (C); 5 μm (whole cell stills), 1 μm (moving vesicle stills), and 10 s and 5 μm (kymographs) (E); 10 μm (I); and 1 s and 5 μm (J).

A MRC5 cells

KIF5B-MDC-GFP

Maximum projection

(1-370) (1-560) (1-807)

TagRFP-MAP2B TagRFP-MAP2B TagRFP-MAP2B

B

C KIF5B-MDC(1-560)-GFP   KIF5B-MDC(1-807)-GFP

Control + MAP2 Control + MAP2

After AMPPNP

TagRFP TagRFP-MAP2B TagRFP TagRFP-MAP2B

D

E

KIF5B

Amino acid 1   560   807 962
560-807

MAP2B

Amino acid 1   160   1351   1825
160-1351
1-1825

KIF1A

Amino acid 1   657   1698
657-1698

F

kDa Input Pull-down IP: GFP-MAP2B (1-1825)
100—
Anti-mCherry
70—
50—
40—
Anti-MAP2
250—

mCherry KIF5B (560-807) mCherry KIF5B (560-807)

G

kDa Input Pull-down IP: GFP-MAP2B (160-1351)
100—
Anti-mCherry
70—
50—
40—
Anti-GFP
250—

mCherry KIF5B (560-807) mCherry KIF5B (560-807)

H

Input Pull-down IP: GFP-MAP2B (1-1825)
100—
Anti-HA
70—
50—
40—
Anti-GFP
250—

KIF1A (657-1698) KIF1A (657-1698)

(legend on next page)

axon (Figures 6B and 6C). Since almost no vesicle reversal events were detected (<0.01%) and axonal branching points were rare, we interpreted that the disappearance of axonal Rab6 vesicles in our experiments was most likely due to docking or exocytotic events along the axon. Quantification revealed that in addition to the reduced number of vesicles leaving the soma, MAP2 depletion also markedly decreased the distribution of anterogradely moving Rab6 vesicles along the rest of the axon (Figure 6C; Table S1C). MAP2 depletion did not significantly affect the number of retrogradely moving vesicles or other motility parameters such as run length, pauses, and pause frequency compared to the controls (Figures S6A–S6E; Tables S1C–S1F). Together these data indicate that MAP2 not only promotes anterograde motility during cargo transit from the soma through the proximal axon but also facilitates the dispersal of vesicles into the more distal regions.

MAP2 Regulates Cargo Velocity by Balancing KIF1 and KIF5 Motor Activities

How does MAP2 promote the dispersal of DCVs into the distal axon? The data from our inducible cargo trafficking assay in MRC5 cells showed that the recruitment of distinct kinesin family members can differentially modulate vesicle velocity (Kapitein et al., 2010) (Figures S5I–S5K). In this way, switching kinesin motors may directly control cargo speeds. Consistently, MRC5 cells expressing different KIF5 and KIF1 motor ratios show an intermediate range of velocities without the dominant influence of one specific kinesin motor, indicating that the final cargo velocity depends on the ratio of motor activities (Figure S5K; Table S1A). We next explored the effect of MAP2 on Rab6 vesicle velocity in DRG axons. In control DRG neurons, the velocity of Rab6 vesicles along the axon varied around the mean value of 2.0 μm/s (Figure 6D; Table S1D). MAP2 knockdown did not affect retrograde velocities (Figure S6B) but markedly reduced anterograde Rab6 velocities (~1.6 μm/s) (Figure 6D). Decreased anterograde velocities were also corroborated for NPY-labeled vesicles after MAP2 depletion (Figures S6F–S6H; Table S1A). We hypothesized that MAP2 regulates the balance between slow KIF5 and fast KIF1 motor activities to drive Rab6 vesicle transport. Accordingly, we inspected the distribution of anterograde velocities of Rab6 vesicles along the whole length of DRG axons (Figure 6E). In the majority of cases, the velocities histogram displayed two clearly distinguishable peaks (Figure 6F). We fitted the velocity profiles with two Gaussians and identified slow and fast velocity subpopulations of Rab6 vesicles (Figure 6F).

Strikingly, whereas the mean velocities of the two sub-populations remained constant, in MAP2-depleted axons we observed an increase in the fraction of slow movements corresponding to enhanced KIF5 motor activity in the distal axon (Figures 6G and 6H). Together our data indicate that MAP2 regulates DCV velocity by balancing KIF5 and KIF1 motor activities.

In MAP2 KO DRG neurons we also observed decreased anterograde Rab6 velocities (Figures S6I, S6J, S6L, and S6M; Table S1A). However, in this case the decrease in vesicle velocity did not correlate with a reduction in the number of axonal entries (Figure S6K). Decomposition analysis of the distribution of anterograde velocities in rat and mouse DRG neurons (Figures S6N and S6O) showed that both MAP2 knockdown (rat) and MAP2 KO (mouse) conditions led to the slowdown of a significant fraction of Rab6 vesicles, confirming the universality of the mechanism (Figures S6P and S6Q). However, in mouse DRG neurons we found an additional population of Rab6 vesicles that move with velocities >2 μm/s. This subpopulation of very fast anterograde Rab6 vesicles is not present in rat neurons and is not affected by MAP2 regulation (Figures S6P and S6Q).

Axonal Cargo Spreading Depends on MAP2-Mediated Regulation of Velocities

To investigate how changes in velocities can lead to changes in DCV distribution in DRG axons, we generated a mathematical model (Figure 6I). We assumed that after cell body exit, DCVs are transported at a constant velocity and that the probability of exocytosis or vesicle docking is the same along the axon. Consistent with the experimental data, the theoretical model showed that the distribution of moving vesicles follows an exponential decay (Figure 6C, dotted lines). Its shape depends only on three parameters: the number of vesicles entering the axon from the soma, the vesicles' velocity, and the exocytosis and docking rate. From the fit we found that the characteristic time of exocytosis and docking was equal to 6 min. According to our model, the vesicles' velocity and the exocytosis and docking rate defined the characteristic "axon penetration" depth of DCVs. In control axons, fast-moving DCVs exocytose or dock farther into the distal axon. In MAP2 depleted axons, however, slower-moving DCVs exocytose or dock in the proximal axon, which corresponds with the observed increase in the number of non-motile DCVs in the proximal axon. Together, the experimental and theoretical findings indicate that MAP2 regulation of cargo velocity is required for the axonal entry

---

Figure 5. Interaction of MAP2 with KIF5 Prevents the Binding of Kinesin to Microtubules

(A) Maximum-intensity projections of TIRF movies of MRC5 cells transfected with the indicated constructs.

(B) Number of projected KIF5 tracks per 100 μm² labeled with the indicated constructs.
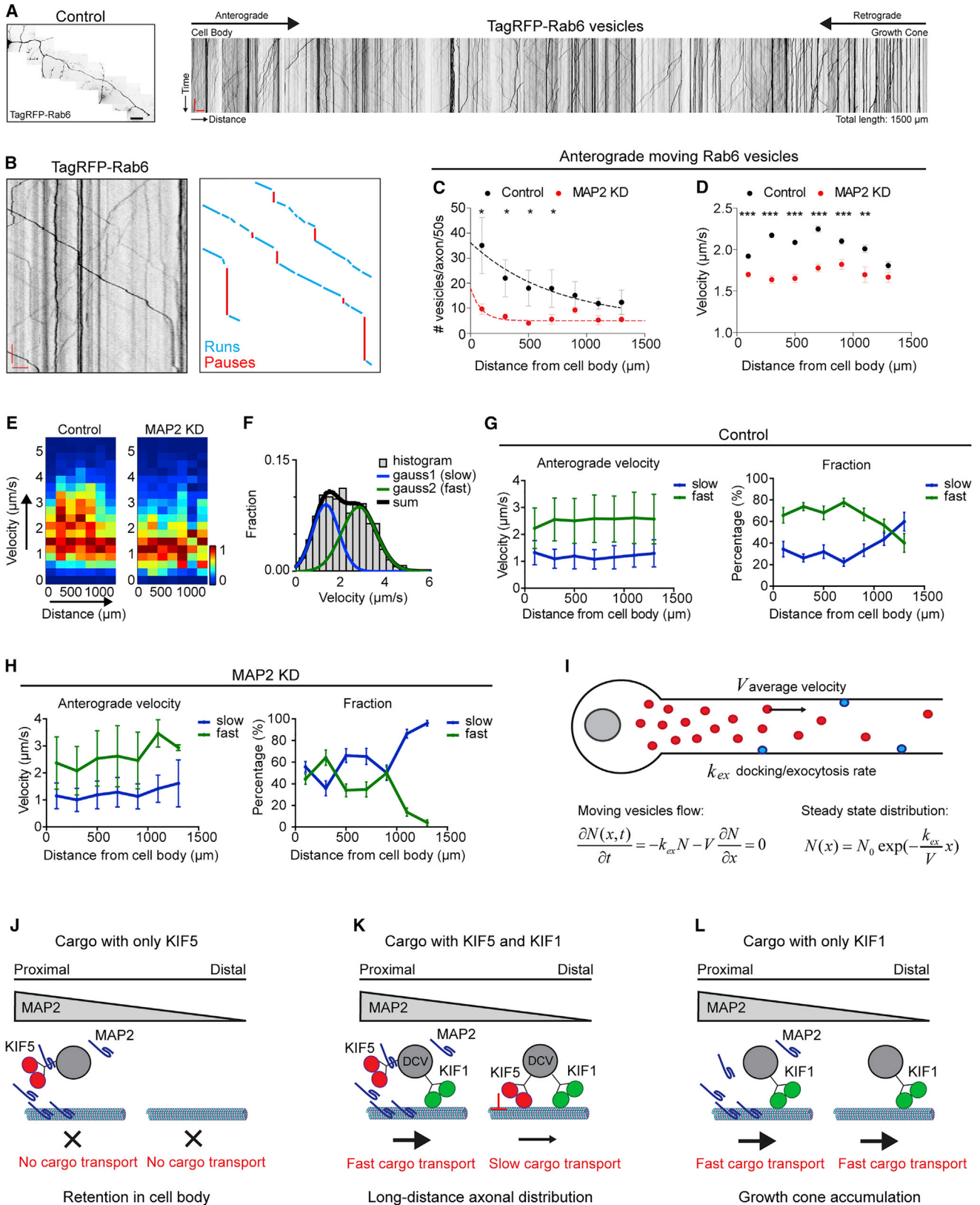
(C) Representative images of COS7 cells expressing the indicated constructs that were untreated or treated with AMPPNP and later fixed. Red arrows, regions of kinesin microtubule binding.

(D) Percentage of cells in which the indicated truncated versions of KIF5B localized to microtubules (MT) after AMPPNP treatment. n = 30 cells per condition from three independent experiments.

(E) Schematics of the indicated constructs. MD, motor domain; CC, coiled-coil; T, tail; proj. C, projection domain common to MAP2C and MAP2B; proj. B, projection domain exclusive to MAP2B; MTBD, microtubule binding domain.

(F–H) Western blot with indicated antibodies of GFP-MAP2B immunoprecipitations.

Mean ± SEM. NS, non-significant; **p < 0.01 (t test; three independent experiments; see Table S1B). Scale bars indicate 10 μm (A) and 20 μm (C).

A Control — TagRFP-Rab6

Anterograde → Cell Body — TagRFP-Rab6 vesicles — Retrograde ← Growth Cone

Time ↕ Distance → Total length: 1500 μm

B TagRFP-Rab6

Runs
Pauses

Anterograde moving Rab6 vesicles

C Control — MAP2 KD
\# vesicles/axon/50s vs Distance from cell body (μm)

D Control — MAP2 KD
Velocity (μm/s) vs Distance from cell body (μm)

E Control — MAP2 KD
Velocity (μm/s) vs Distance (μm)

F histogram — gauss1 (slow) — gauss2 (fast) — sum
Fraction vs Velocity (μm/s)

G Control

Anterograde velocity — slow / fast
Velocity (μm/s) vs Distance from cell body (μm)

Fraction — slow / fast
Percentage (%) vs Distance from cell body (μm)

H MAP2 KD

Anterograde velocity — slow / fast
Velocity (μm/s) vs Distance from cell body (μm)

Fraction — slow / fast
Percentage (%) vs Distance from cell body (μm)

I V average velocity

k_{ex} docking/exocytosis rate

Moving vesicles flow:

$$\frac{\partial N(x,t)}{\partial t} = -k_{ex}N - V\frac{\partial N}{\partial x} = 0$$

Steady state distribution:

$$N(x) = N_0 \exp\left(-\frac{k_{ex}}{V}x\right)$$

J Cargo with only KIF5

Proximal — Distal

MAP2

KIF5 — MAP2

No cargo transport — No cargo transport

Retention in cell body

K Cargo with KIF5 and KIF1

Proximal — Distal

MAP2

KIF5 — DCV — MAP2 — KIF1 — DCV — KIF5 — KIF1

Fast cargo transport — Slow cargo transport

Long-distance axonal distribution

L Cargo with only KIF1

Proximal — Distal

MAP2

MAP2 — KIF1 — KIF1

Fast cargo transport — Fast cargo transport

Growth cone accumulation

(legend on next page)

and long-distance transport and distribution of DCVs in DRG axons.

DISCUSSION

Adult DRG Neurons Lack a Classical Structured AIS in the Proximal Axon

The idea of a sorting mechanism for selective axonal entry in DRG neurons comes from findings showing that adhesion molecules or secretory vesicles are enriched in axons (Kamiguchi and Lemmon, 1998; Zhao et al., 2011), whereas lysosome or mRNAs mostly accumulate in the soma (Gumy et al., 2011). Several studies have shown that selective cargo trafficking largely depends on the AIS (Leterrier and Dargent, 2014). However, we were unable to detect a structured AIS in the proximal axon of adult DRG neurons in vitro and in vivo. Previous studies have shown that AIS markers are enriched in DRG neurons in culture, although these components have only been found enriched in the proximal axon of in vitro co-culture systems of embryonic DRG neurons and myelinating Schwann cells (Hedstrom et al., 2007). For example, in DRG neurons neurofascin is initially uniformly distributed along the axon (Dzhashiashvili et al., 2007) and, upon induction of myelination, becomes increasingly apparent in the proximal segment around the first node of Ranvier. Without myelinating Schwann cells, AIS components remain diffuse in DRG axons (Ching et al., 1999). Thus, it appears that a structured AIS does not spontaneously form in the proximal axon of non-myelinated DRG neurons in culture, in sharp contrast to hippocampal neurons, for example. These findings are consistent with reports showing that mature DRG neurons do not initiate action potentials in the proximal axon (Martini, 2011). One possibility is that in DRG neurons the enriched AIS markers do not localize to the proximal axon but instead more distally, near the axonal bifurcation region. We specifically inspected DRG neurons that presented pseudounipolar morphology in culture and analyzed distal parts of axons in DRGs in vivo. Structured AIS markers were absent in pseudounipolar DRGs in vitro. In vivo, the majority of DRG proximal axons were labeled with TRIM46 but were Ankyrin G negative and could be traced back to the soma. Ankyrin G enrichment in the DRG proximal axon has been described in vivo (Brandao et al., 2012); however, we found that, only very rarely (<2%), proximal axons contained stretches of Ankyrin G staining.

MAP2 Defines the Pre-axonal Filtering Region for Axonal Cargo Entry

Recent studies have shown alternative mechanisms for the selective sorting of axonal cargos (Petersen et al., 2014; Farías et al., 2015; Kuijpers et al., 2016). We found that MAP2 localization to the proximal axon is TRIM46 dependent, as observed in hippocampal neurons (van Beuningen et al., 2015). Given that the compartmentalization of MAP2 and TRIM46 is conserved in both hippocampal and DRG neurons, it is tempting to speculate that these two microtubule-binding proteins establish a critical cargo-sorting region within the proximal axon of various neuronal cell types. To determine whether MAP2 plays a role in regulating axonal cargo filtering, we analyzed the effect of MAP2 on the axonal distribution of a broad variety of cellular organelles that present multiple combinations of motor protein-cargo complexes. We were intrigued by the finding that MAP2 depletion produced different outcomes for different organelles. This suggested that MAP2 was involved in regulating motor protein activity. Indeed, MAP2 prevented lysosomes from leaving the cell body but simultaneously facilitated the fast and uninterrupted exit of DCVs from the soma. KIF5 has been reported as the predominant motor for lysosomal transport (Rosa-Ferreira and Munro, 2011). The fact that lysosomal axonal transport increases after MAP2 depletion suggested that MAP2 might be inhibiting KIF5 motor activity. Since, under normal conditions, the majority of lysosomes reside in the cell body, we turned to analyze the axonal trafficking of DCVs. DCV trafficking is a very-well-characterized microtubule-based transport route found in many different types of neurons in many model organisms (Lo et al., 2011; Wong et al., 2012). Previous reports have shown that kinesin-1 (KIF5) and kinesin-3 (KIF1) family members are involved in the transport of DCVs, which are predominantly present in hippocampal and DRG axons and transported over long distances in both anterograde and retrograde directions (Schlager et al., 2014). Thus,

Figure 6. Axonal Transport of Dense Core Vesicles Depends on MAP2-Mediated Regulation of Velocities

(A) (Left) Image of a full-length control adult DRG neuron (DIV4) expressing TagRFP-Rab6. Overlapping images were stitched together. (Right) Kymographs of a full-length control adult DRG axon ranging from the cell body to the growth cone. Overlapping kymographs were stitched together to show the extent of vesicle dynamics at different points along the axon.

(B) Representative kymograph of TagRFP-Rab6 behavior in the axon of an adult DRG neuron. Highlighted projections of the kymograph represent the parameters quantified.

(C) Number of anterograde moving TagRFP-Rab6 vesicles in full-length control and MAP2 knockdown adult DRG axons (DIV4) (dots, experimental data) and the corresponding fittings of the mathematical model (I) (dotted lines) (n = 8 axons respectively).

(D) Anterograde mean velocity of TagRFP-Rab6 vesicles in full-length control and MAP2 knockdown adult DRG axons (DIV4) (n = 8 axons respectively; for measurement details, see Table S1).

(E) Color map showing the distribution of anterograde velocities along control or MAP2 knockdown whole DRG axons.

(F) Representative histogram showing the distribution of velocities in a DRG axon (bars). Fitting with a sum of two Gaussians was used to highlight slow- and fast-velocity populations within the distribution (curves).

(G and H) Anterograde Rab6 velocity distribution decomposition into fast and slow fractions along the full length of control (G) (n = 8) and MAP2 knockdown (H) (n = 8) DRG axons. Error bars at velocities' plots represent standard deviations of fitted Gaussian distributions; error bars at fractions' plots are the errors of the fit.

(I) Schematic and main equations of the mathematical model of anterograde Rab6 vesicle distribution in DRG axons. Vesicles emanate from the cell body, move along the axon and have a constant probability of docking or exocytosis.

(J–L) Graphic model showing how MAP2 regulation of kinesin motor activities leads to cargo sorting and trafficking in adult DRG axons.

Mean ± SEM (except G and H). *p < 0.05 (Mann-Whitney test; three independent experiments) (C); ***p < 0.001; **p < 0.01 (t test; three independent experiments) (D). Scale bars indicate (left) 100 μm and (right) 20 s and 10 μm (A), and 5 s and 2.5 μm (B).

MAP2-dependent KIF1 versus KIF5 cargo filtering in the proximal axon could be a universal cargo-sorting mechanism in neurons. However, we exclude the possibility that MAP2 is redundant with the role of the AIS in the central nervous system (CNS). CNS neurons possess more specialized compartments (i.e., dendrites) than DRG neurons, which likely require additional layers of traffic control. For example, we have shown the importance of the AIS in acting as a barrier for dendritic cargo transport (Kuijpers et al., 2016). Most likely, the AIS and MAP2 are two parallel mechanisms to regulate axonal cargo sorting—the AIS for axonal and dendritic cargo sorting and MAP2 for filtering axonal cargo entries. In CNS neurons, MAP2 predominantly labels the somatodendritic compartment, raising the question of how MAP2 affects secretory vesicle cargo trafficking in dendrites. Previous studies have shown that KIF5 does not drive cargo transport (Kapitein et al., 2010) and that KIF1 is the primary motor to drive DCV trafficking into dendrites (Lipka et al., 2016). These data support our model showing that MAP2 impairs KIF5 and favors KIF1-driven DCV transport.

MAP2 Controls the Axonal Growth Potential of Neurons

Our data indicate that MAP2 knockdown increases the axonal growth potential of adult DRG and hippocampal neurons. Thus, it appears that perturbing soma-axon trafficking has a general strong effect on the neuron's axonal length-sensing process (Albus et al., 2013). MAP2 knockdown may not only interfere with secretory vesicle transport but may also reduce the trafficking of inhibitory factors involved in controlling axonal outgrowth. Alternatively, increased exocytosis of vesicles in the cell body (due to secretory defects) or membrane insertion at aberrant locations along the axon might have a stronger neurite outgrowth effect compared to membrane insertion in distal axons. In addition, motor-dependent mRNA localization may regulate axonal growth. In this context we found that MAP2 depletion favored the transport of the RNA-binding protein ZBP1 into the axon. Interestingly, ZBP1 was previously shown to support the axonal growth potential of DRG neurons (Donnelly et al., 2011). In young DRG neurons, MAP2 does not strongly localize to the proximal axon, and its depletion does not affect the axonal growth potential of embryonic DRGs (data not shown). Thus, MAP2 appears to play a specific role in adult neurons, but not during development. Indeed, a strong developmental phenotype was not observed in the MAP2 KO mouse model. Other MAPs could be compensating for the loss of MAP2 in developing DRGs. For instance, MAP1B is expressed prominently during early stages of neuronal development, and the MAP2/MAP1B double KO mice die in their perinatal period (Teng et al., 2001). A possibility is high-functional redundancy among MAPs during development with synergistic functions in vivo. Our study suggests that in adult DRG neurons a physiologically relevant phenotype might be displayed under acute conditions. As proof of principle, we examined the axonal growth potential of MAP2 KO mice and indeed found a strong increase in axonal outgrowth. Since the enhanced axonal growth effect is only shown under in vitro culture conditions, a more detailed analysis of the in vivo role of MAP2 in adult sensory neurons is required. In particular, future studies should further investigate the role of MAP2 during axon regeneration in various in vivo nerve injury models. This study suggests that MAP2 is a gatekeeper of axonal growth capacity via regulation of axonal cargo trafficking in adult DRG neurons.

MAP2 Prevents the Binding of KIF5 to Microtubules to Regulate Axonal Cargo Transport

We found that KIF5 cannot drive cargo transport in the presence of MAP2 and that the coiled-coil region KIF5(560–807) is responsible for this inhibiting effect. The cargo-binding domain is not in the second coiled-coil region (560–807) but in the more C-terminal part of the tail region between amino acids 828 and 962 (Randall et al., 2013). Therefore, we hypothesized that MAP2 might disrupt the microtubule binding affinity of KIF5 rather than its capacity to bind to cargos. In non-neuronal cells we confirmed that MAP2 prevents the landing of KIF5 on microtubules. In DRG neurons, we still observed some KIF5 decoration of microtubules, although no motility events could be detected. Interaction of the projection domain of MAP2 with the second coiled coil of KIF5 might exert repulsive forces that disrupt the binding of kinesin with microtubules. This is in accordance with previous in vitro studies suggesting that the projection domain of MAP2 inhibits the landing of KIF5 on microtubules by steric hindrance (Lopez and Sheetz, 1993). We found that activity-dependent MAP2 dephosphorylation in DRG neurons led to a strong increase in the number of axonal cargo entries, suggesting that the phosphorylation state of MAP2 might modulate its interaction with KIF5 and hence cargo transport. Interestingly, we also found that MAP2 is largely cytosolic and mobile, colocalizes with Rab6 vesicles, and can be recruited to moving cargos in the presence of KIF5. The interaction of MAP2 with KIF5 on the cargo might persist beyond the MAP2 pre-axonal region. Gradual turnover of MAP2 on these vesicles would allow the delayed re-activation of KIF5, which subsequently decreases KIF1-driven motility in distal axons. In this line, we observed an increase in the fraction of slow cargo velocities along the axon beyond the proximal segment.

Balancing KIF5 and KIF1 Motor Activities Drives Long-Distance Cargo Transport

Recent studies show that diverse kinesin motors attached to the same cargo work in teams to coordinate efficient antero-grade transport (Arpağ et al., 2014; Schlager et al., 2014). Most cargos, including DCVs, have more than one type of motor attached at any given time (Grigoriev et al., 2007). This means that, for example, one single Rab6 vesicle can present both fast (KIF1) and slow (KIF5) runs during any period of time, depending on which motor is active. We found that MAP2 inhibits the activity of KIF5 on DCVs, thus changing the balance between fast- and slow-moving vesicles along the full length of the axon. Our model implies that when MAP2 impairs the activity of KIF5, KIF1, which is attached to the same vesicle, will be the main kinesin responsible for the motility of that vesicle. Indeed, the fact that both motors are attached to the vesicle can be seen from the kymographs, where fast and slow run alternately. An increase in the average velocity correlates with an increase in the number of fast runs, which in turn

report on the activity of KIF1. It has been suggested that cargo motility can also be regulated by microtubule binding proteins, which can subsequently coordinate the activity of one or more motor proteins (Atherton et al., 2013). For instance, the effective cooperation between two anterograde motors displaying fast and slow velocities has also been reported in cilia (Prevo et al., 2015). By analogy with secretory vesicle trafficking in fibroblast cells (Grigoriev et al., 2007), we found that a combination of kinesin-1 (~1.0 um/s, slow) and kinesin-3 (~2.0 um/s, fast) family members can regulate DCV motility in DRG neurons. We also show that in MRC5 cells, simultaneous recruitment of different ratios of KIF1 and KIF5 motors causes intermediate cargo velocities. Although none of the motors appear to dominate, small amounts of KIF5 slow down the velocity of cargo in the presence of higher numbers of KIF1. In DRG neurons, depletion of KIF1 prevents Rab6 vesicles from leaving the cell body, whereas disruption of KIF5 leads to the rapid accumulation of vesicles at the growth cone, suggesting that KIF1 predominately drives cargo exit from the soma. We propose a general model in which the regulation of the cooperative action of multiple kinesin motors is a fundamental mechanism for proper axonal cargo entry and distribution (Figures 6J–6L).

In summary, we propose that selective cargo sorting and transport in DRG neurons depend on the newly discovered MAP2-defined pre-axonal filtering zone. Since MAP2 is also present in other neuronal cell types, our findings reveal a general mechanism for the regulation of cargo trafficking, which depends on two basic elements: compartmentalized MAPs and kinesin motors. Given that alterations in cargo trafficking pathways have been described in several neurodegenerative diseases, our findings provide new molecular targets to investigate the axonal trafficking machinery in neuropathological disease models.

STAR★METHODS

Detailed methods are provided in the online version of this paper and include the following:

- KEY RESOURCES TABLE
- CONTACT FOR REAGENT AND RESOURCE SHARING
- EXPERIMENTAL MODEL AND SUBJECT DETAILS
  - Animals
  - Hippocampal neuron culture and transfection
  - Cortical neuron culture and transfection
  - DRG neuron culture and transfection
  - COS7 and MRC5 cell culture and transfection
- METHOD DETAILS
  - DNA and shRNA constructs
  - Preparation of tissue extracts and Immunoblotting
  - GFP Immunoprecipitation
  - Microtubule binding assay in fixed COS7 cells
  - Hippocampal and DRG Neuron Immunofluorescence
  - Whole DRG Immunohistochemistry
  - Epifluorescence microscopy
  - Confocal microscopy
  - Laser Scanning Confocal and STED microscopy

- Live-cell imaging
- Image analysis and quantification
- Mathematical model describing the spreading of vesicles in the axon
- QUANTIFICATION AND STATISTICAL ANALYSIS

REFERENCES

Albus, C.A., Rishal, I., and Fainzilber, M. (2013). Cell length sensing for neuronal growth control. Trends Cell Biol. 23, 305–310.

Arpağ, G., Shastry, S., Hancock, W.O., and Tüzel, E. (2014). Transport by populations of fast and slow kinesins uncovers novel family-dependent motor characteristics important for in vivo function. Biophys. J. 107, 1896–1904.

Atherton, J., Houdusse, A., and Moores, C. (2013). MAPping out distribution routes for kinesin couriers. Biol. Cell 105, 465–487.

Brandao, K.E., Dell'Acqua, M.L., and Levinson, S.R. (2012). A-kinase anchoring protein 150 expression in a specific subset of TRPV1- and CaV 1.2-positive nociceptive rat dorsal root ganglion neurons. J. Comp. Neurol. 520, 81–99.

Ching, W., Zanazzi, G., Levinson, S.R., and Salzer, J.L. (1999). Clustering of neuronal sodium channels requires contact with myelinating Schwann cells. J. Neurocytol. 28, 295–301.

Dehmelt, L., and Halpain, S. (2005). The MAP2/Tau family of microtubule-associated proteins. Genome Biol. 6, 204.

Donnelly, C.J., Willis, D.E., Xu, M., Tep, C., Jiang, C., Yoo, S., Schanen, N.C., Kirn-Safran, C.B., van Minnen, J., English, A., et al. (2011). Limited availability of ZBP1 restricts axonal mRNA localization and nerve regeneration capacity. EMBO J. 30, 4665–4677.

Dzhashiashvili, Y., Zhang, Y., Galinska, J., Lam, I., Grumet, M., and Salzer, J.L. (2007). Nodes of Ranvier and axon initial segments are ankyrin G-dependent domains that assemble by distinct mechanisms. J. Cell Biol. 177, 857–870.

Farías, G.G., Guardia, C.M., Britt, D.J., Guo, X., and Bonifacino, J.S. (2015). Sorting of dendritic and axonal vesicles at the pre-axonal exclusion zone. Cell Rep. *13*, 1221–1232.

Grigoriev, I., Splinter, D., Keijzer, N., Wulf, P.S., Demmers, J., Ohtsuka, T., Modesti, M., Maly, I.V., Grosveld, F., Hoogenraad, C.C., and Akhmanova, A. (2007). Rab6 regulates transport and targeting of exocytotic carriers. Dev. Cell *13*, 305–314.

Gumy, L.F., Yeo, G.S.H., Tung, Y.-C.L., Zivraj, K.H., Willis, D., Coppola, G., Lam, B.Y.H., Twiss, J.L., Holt, C.E., and Fawcett, J.W. (2011). Transcriptome analysis of embryonic and adult sensory axons reveals changes in mRNA repertoire localization. RNA *17*, 85–98.

Hagiwara, H., Yorifuji, H., Sato-Yoshitake, R., and Hirokawa, N. (1994). Competition between motor molecules (kinesin and cytoplasmic dynein) and fibrous microtubule-associated proteins in binding to microtubules. J. Biol. Chem. *269*, 3581–3589.

Hammond, J.W., Blasius, T.L., Soppina, V., Cai, D., and Verhey, K.J. (2010). Autoinhibition of the kinesin-2 motor KIF17 via dual intramolecular mechanisms. J. Cell Biol. *189*, 1013–1025.

Hedstrom, K.L., Xu, X., Ogawa, Y., Frischknecht, R., Seidenbecher, C.I., Shrager, P., and Rasband, M.N. (2007). Neurofascin assembles a specialized extracellular matrix at the axon initial segment. J. Cell Biol. *178*, 875–886.

Hedstrom, K.L., Ogawa, Y., and Rasband, M.N. (2008). AnkyrinG is required for maintenance of the axon initial segment and neuronal polarity. J. Cell Biol. *183*, 635–640.

Hernández, M.A., Avila, J., Moya, F., and Alberto, C. (1989). Rearrangement of microtubule associated protein parallels the morphological transformation of neurons from dorsal root ganglion. Neuroscience *29*, 471–477.

Jaworski, J., Kapitein, L.C., Gouveia, S.M., Dortland, B.R., Wulf, P.S., Grigoriev, I., Camera, P., Spangler, S., Di Stefano, P., Demmers, J., et al. (2009). Dynamic microtubules regulate dendritic spine morphology and synaptic plasticity. Neuron *61*, 85–100.

Kamiguchi, H., and Lemmon, V. (1998). A neuronal form of the cell adhesion molecule L1 contains a tyrosine-based signal required for sorting to the axonal growth cone. J. Neurosci. *18*, 3749–3756.

Kapitein, L.C., and Hoogenraad, C.C. (2011). Which way to go? Cytoskeletal organization and polarized transport in neurons. Mol. Cell. Neurosci. *46*, 9–20.

Kapitein, L.C., and Hoogenraad, C.C. (2015). Building the Neuronal Microtubule Cytoskeleton. Neuron *87*, 492–506.

Kapitein, L.C., Schlager, M.A., Kuijpers, M., Wulf, P.S., van Spronsen, M., MacKintosh, F.C., and Hoogenraad, C.C. (2010). Mixed microtubules steer dynein-driven cargo transport into dendrites. Curr. Biol. *20*, 290–299.

Kapitein, L.C., Yau, K.W., Gouveia, S.M., van der Zwan, W.A., Wulf, P.S., Keijzer, N., Demmers, J., Jaworski, J., Akhmanova, A., and Hoogenraad, C.C. (2011). NMDA receptor activation suppresses microtubule growth and spine entry. J. Neurosci. *31*, 8194–8209.

Kuijpers, M., van de Willige, D., Freal, A., Chazeau, A., Franker, M.A., Hofenk, J., Rodrigues, R.J.C., Kapitein, L.C., Akhmanova, A., Jaarsma, D., and Hoogenraad, C.C. (2016). Dynein regulator NDEL1 controls polarized cargo transport at the axon initial segment. Neuron *89*, 461–471.

Leterrier, C., and Dargent, B. (2014). No Pasaran! Role of the axon initial segment in the regulation of protein transport and the maintenance of axonal identity. Semin. Cell Dev. Biol. *27*, 44–51.

Lipka, J., Kapitein, L.C., Jaworski, J., and Hoogenraad, C.C. (2016). Microtubule-binding protein doublecortin-like kinase 1 (DCLK1) guides kinesin-3-mediated cargo transport to dendrites. EMBO J. *35*, 302–318.

Lo, K.Y., Kuzmin, A., Unger, S.M., Petersen, J.D., and Silverman, M.A. (2011). KIF1A is the primary anterograde motor protein required for the axonal transport of dense-core vesicles in cultured hippocampal neurons. Neurosci. Lett. *491*, 168–173.

Lopez, L.A., and Sheetz, M.P. (1993). Steric inhibition of cytoplasmic dynein and kinesin motility by MAP2. Cell Motil. Cytoskeleton *24*, 1–16.

Maday, S., Twelvetrees, A.E., Moughamian, A.J., and Holzbaur, E.L.F. (2014). Axonal transport: cargo-specific mechanisms of motility and regulation. Neuron *84*, 292–309.

Malet, M., and Brumovsky, P.R. (2015). VGLUTs and glutamate synthesis-focus on DRG neurons and pain. Biomolecules *5*, 3416–3437.

Martini, F.H. (2011). Fundamentals of Anatomy and Physiology, Ninth Edition (Pearson Education).

Matanis, T., Akhmanova, A., Wulf, P., Del Nery, E., Weide, T., Stepanova, T., Galjart, N., Grosveld, F., Goud, B., De Zeeuw, C.I., et al. (2002). Bicaudal-D regulates COPI-independent Golgi-ER transport by recruiting the dynein-dynactin motor complex. Nat. Cell Biol. *4*, 986–992.

Petersen, J.D., Kaech, S., and Banker, G. (2014). Selective microtubule-based transport of dendritic membrane proteins arises in concert with axon specification. J. Neurosci. *34*, 4135–4147.

Prevo, B., Mangeol, P., Oswald, F., Scholey, J.M., and Peterman, E.J.G. (2015). Functional differentiation of cooperating kinesin-2 motors orchestrates cargo import and transport in C. elegans cilia. Nat. Cell Biol. *17*, 1536–1545.

Quinlan, E.M., and Halpain, S. (1996). Postsynaptic mechanisms for bidirectional control of MAP2 phosphorylation by glutamate receptors. Neuron *16*, 357–368.

Randall, T.S., Moores, C., and Stephenson, F.A. (2013). Delineation of the TRAK binding regions of the kinesin-1 motor proteins. FEBS Lett. *587*, 3763–3769.

Rosa-Ferreira, C., and Munro, S. (2011). Arl8 and SKIP act together to link lysosomes to kinesin-1. Dev. Cell *21*, 1171–1178.

Sánchez, C., Díaz-Nido, J., and Avila, J. (2000). Phosphorylation of microtubule-associated protein 2 (MAP2) and its relevance for the regulation of the neuronal cytoskeleton function. Prog. Neurobiol. *61*, 133–168.

Schlager, M.A., Kapitein, L.C., Grigoriev, I., Burzynski, G.M., Wulf, P.S., Keijzer, N., de Graaff, E., Fukuda, M., Shepherd, I.T., Akhmanova, A., and Hoogenraad, C.C. (2010). Pericentrosomal targeting of Rab6 secretory vesicles by Bicaudal-D-related protein 1 (BICDR-1) regulates neuritogenesis. EMBO J. *29*, 1637–1651.

Schlager, M.A., Serra-Marques, A., Grigoriev, I., Gumy, L.F., Esteves da Silva, M., Wulf, P.S., Akhmanova, A., and Hoogenraad, C.C. (2014). Bicaudal d family adaptor proteins control the velocity of Dynein-based movements. Cell Rep. *8*, 1248–1256.

Song, A.-H., Wang, D., Chen, G., Li, Y., Luo, J., Duan, S., and Poo, M.-M. (2009). A selective filter for cytoplasmic transport at the axon initial segment. Cell *136*, 1148–1160.

Taylor, J.R. (1997). An Introduction to Error Analysis: The Study of Uncertainties in Physical Measurements, 2nd Edition (University Science Books).

Teng, J., Takei, Y., Harada, A., Nakata, T., Chen, J., and Hirokawa, N. (2001). Synergistic effects of MAP2 and MAP1B knockout in neuronal migration, dendritic outgrowth, and microtubule organization. J. Cell Biol. *155*, 65–76.

van Beuningen, S.F.B., Will, L., Harterink, M., Chazeau, A., van Battum, E.Y., Frias, C.P., Franker, M.A., Katrukha, E.A., Stucchi, R., Vocking, K., et al. (2015). TRIM46 controls neuronal polarity and axon specification by driving the formation of parallel microtubule arrays. Neuron *88*, 1208–1226.

van Spronsen, M., Mikhaylova, M., Lipka, J., Schlager, M.A., van den Heuvel, D.J., Kuijpers, M., Wulf, P.S., Keijzer, N., Demmers, J., Kapitein, L.C., et al. (2013). TRAK/Milton motor-adaptor proteins steer mitochondrial trafficking to axons and dendrites. Neuron *77*, 485–502.

Wong, M.Y., Zhou, C., Shakiryanova, D., Lloyd, T.E., Deitcher, D.L., and Levitan, E.S. (2012). Neuropeptide delivery to synapses by long-range vesicle circulation and sporadic capture. Cell *148*, 1029–1038.

Zhao, B., Wang, H.-B., Lu, Y.-J., Hu, J.-W., Bao, L., and Zhang, X. (2011). Transport of receptors, receptor signaling complexes and ion channels via neuropeptide-secretory vesicles. Cell Res. *21*, 741–753.

STAR★METHODS

KEY RESOURCES TABLE

REAGENT or RESOURCE	SOURCE	IDENTIFIER
Antibodies		
Mouse monoclonal anti-MAP2 (clone HM-2)	SIGMA	M9942
Goat polyclonal anti-MAP1A (clone N-18)	Santa Cruz	sc-8969
Goat polyclonal anti-MAP1B (clone N-19)	Santa Cruz	sc-8970
Rabbit polyclonal anti-βIV-Spectrin	Matthew Rasband	N/A
Mouse monoclonal anti-Rab6A	Matanis et al., 2002	N/A
Mouse monoclonal anti-TRIM46	van Beuningen et al., 2015	N/A
Rabbit polyclonal anti-EB3	Jaworski et al., 2009	N/A
Mouse monoclonal anti-mCherry	Clontech	632543
Rabbit polyclonal anti-GFP	MBL	598
Mouse monoclonal anti-AnkG (clone 4G3F8)	Life Technologies	33-8800
Rabbit polyclonal anti-MAP2	Cell Signaling	4542
Guinea pig polyclonal anti-MAP2	Synaptic Systems	188004
Mouse monoclonal anti-phosporylated MAP2 (clone AP18)	Thermofisher	MA5-12826
Rabbit polyclonal anti-Neurofilament L (clone C28E10)	Cell Signaling	2837
Rabbit polyclonal anti-βIII-tubulin	Covance	PRB-435P
Mouse monoclonal anti-βIII-tubulin (clone TUJ1)	SIGMA	T8660
Rabbit polyclonal anti-MAP4 (clone H300)	Santa Cruz	sc-67152
Goat polyclonal anti-MAP7 (clone T-17)	Santa Cruz	sc-161824
Goat polyclonal anti-MAP9 (clone D-18)	Santa Cruz	sc-164961
Mouse monoclonal anti-pan-Neurofascin (clone L11A/41)	NeuroMab/Antibodies Incorporated	75-027
Mouse monoclonal anti-pan-Nav (clone K58/35)	SIGMA	S8809
Mouse monoclonal anti-alpha-tubulin (clone B-5-1-2)	SIGMA	T5168
Rabbit polyclonal anti-TRIM46	van Beuningen et al., 2015	N/A
Rabbit polyclonal anti-KIF1Bβ	Bethyl	A301-055A
Rabbit polyclonal anti-KIF1C	Cytoskeleton	AKIN11
Anti-mouse Alexa488	Life Technologies	A11029
Anti-rabbit Alexa488	Life Technologies	A11034
Anti-mouse Alexa568	Life Technologies	A11031
Anti-rabbit Alexa568	Life Technologies	A11036
Anti-mouse Cy3	Jackson ImmunoResearch	715-165-150
Anti-rabbit Cy3	Jackson ImmunoResearch	711-165-152
Anti-mouse Cy5	Jackson ImmunoResearch	ab6563
Anti-rabbit Cy5	Jackson ImmunoResearch	ab6564
Anti-mouse anti-HRP	DAKO	P0260
Anti-rabbit anti-HRP	DAKO	P0399
Chemicals, Peptides, and Recombinant Proteins		
Rapalog heterodimerizer	Ariad	AP21967
Microtubule-associated protein rich fraction from bovine brain (referred as MAP fraction)	Cytoskeleton	MAPF-A
Non-hydrolyzable ATP analogue AMPPNP	SIGMA	A2647
Streptolysin-O (SLO)	SIGMA	S5265
GFP-Trap magnetic beads	Chromotek	gtm-20
Fugene6	Promega	E2691

(*Continued on next page*)

REAGENT or RESOURCE	SOURCE	IDENTIFIER
Lipofectamine 2000	Thernofisher	11668019
Fluorsave mounting medium	EMD Millipore	345789
Vectashield mounting medium	Vectorlabs	H-1000
Critical Commercial Assays		
Neon transfection system 10 uL kit	Thermofisher	MPK1025
Rat Neuron Nucleofector kit	Amaxa	VVPG-1003
Experimental Models: Cell Lines		
Human MRC5	ATCC	CCL-171
Human HEK293	ATCC	CRL1651
Monkey COS7	ATCC	CRL1573
Experimental Models: Organisms/Strains		
Primary hippocampal cultures from rat E18 brains	N/A	N/A
Dissociated DRG neurons isolated from adult female Wistar rats (3–5 months old)	N/A	N/A
Dissociated DRG neurons isolated from adult wild type C57BL/6 mice (3–5 months old)	N/A	N/A
Dissociated DRG neurons isolated from adult MAP2 KO mice (3–5 months old)	gift of N. Hirokawa	N/A
Recombinant DNA		
GFP-MAP2B (HMW)	This paper	N/A
GFP-MAP2C (LMW)	Kapitein et al., 2011	N/A
GFP-Rab6	Schlager et al., 2014	N/A
TagRFP-Rab6	Schlager et al., 2014	N/A
GFP-KIF5B-tail (dominant negative)	van Spronsen et al., 2013	N/A
HA-KIF5B-MDC(1-807)-FRB	Kapitein et al., 2010	N/A
KIF5B-MDC(1-807)-GFP-FRB	van Spronsen et. al., 2013	N/A
HA-KIF1C-MDC(1-397)-FRB	Kapitein et al., 2010	N/A
PEX-mRFP-FKBP	Kapitein et al., 2010	N/A
mCherry-Rab6-FKBP	Schlager et al., 2014	N/A
NPY-venus	Grigoriev et al., 2007	N/A
GFP-MT+Tip	Kapitein et al., 2010	N/A
TagRFP-MAP2B	This paper	N/A
HA-KIF5B-MDC-(1-370)-FRB	This paper	N/A
HA-KIF5B-MDC-(1-560)-FRB	This paper	N/A
KIF5B-MDC(1-370)-GFP-FRB	This paper	N/A
KIF5B-MDC(1-560)-GFP-FRB	This paper	N/A
mCherry-KIF5B(560-807)	This paper	N/A
HA-KIF1A(657-1698)	This paper	N/A
NPY-RFP	This paper	N/A
GFP-MAP2B(160-1351)	This paper	N/A
MAP2-shRNA #1	Kapitein et al., 2010	N/A
MAP2-shRNA #2	Kapitein et al., 2010	N/A
TRIM46-shRNA #1	van Beuningen et al., 2015	N/A
TRIM46-shRNA #2	van Beuningen et al., 2015	N/A
KIF1A-shRNA	Lipka et al., 2016	N/A
KIF1B-shRNA	Lipka et al., 2016	N/A
KIF1C-shRNA	Lipka et al., 2016	N/A
Neurofilament-L-shRNA #1: UGGACAUUGAGAUUGCAGC	This paper	N/A

Continued		
REAGENT or RESOURCE	SOURCE	IDENTIFIER
Neurofilament-L-shRNA #2: GUCAAGAUGGCAUUGGACA	This paper	N/A
Neurofilament-L-shRNA #3: CGCCUACUUAAGGCUAAGA	This paper	N/A
Software and Algorithms		
ImageJ	NIH	https://imagej.nih.gov/ij/
GraphPad Prism	GraphPad Software INC	http://www.graphpad.com/scientific-software/

CONTACT FOR REAGENT AND RESOURCE SHARING

Further information and requests for resources and reagents should be directed to and will be fulfilled by Casper Hoogenraad (c.hoogenraad@uu.nl).

EXPERIMENTAL MODEL AND SUBJECT DETAILS

Animals
All experiments with animals were performed in compliance with the guidelines for the welfare of experimental animals issued by the Government of the Netherlands, and were approved by the Animal Ethical Review Committee (DEC) of the Erasmus MC and Utrecht University.

Hippocampal neuron culture and transfection
Primary hippocampal cultures were prepared from embryonic day 18 (E18) rat brains (van Beuningen et al., 2015). Cells were plated on coverslips coated with poly-L-lysine (30 μg/ml) and laminin (2 μg/ml) at a density of 75,000/well. Hippocampal cultures were grown in Neurobasal medium (NB) supplemented with B27, 0.5 mM glutamine, 12.5 μM glutamate and penicillin/streptomycin. Hippocampal neurons were transfected using Lipofectamine 2000 (ThermoFisher). Briefly, DNA (3.6 μg/well) was mixed with 3 μl Lipofectamine 2000 in 200 μl NB, incubated for 30 minutes and then added to the neurons in NB at 37 °C in 5% CO2 for 45 min. Next, neurons were washed with NB then incubated in the original medium at 37 °C in 5% CO2.

Cortical neuron culture and transfection
Primary cortical neurons were isolated from E18 rat brain (van Beuningen et al., 2015). Cells (1 × 10^6) were transfected using the Amaxa Rat Neuron Nucleofector kit (Lonza) with 3 μg of plasmid DNA and plated in 6-well plates (5 × 10^5 cells/well) coated with poly-L-lysine (37.5 μg/ml) and laminin (5 μg/ml) containing DMEM supplemented with 10% FBS as described previously (van Beuningen et al., 2015). Cells were allowed to recover and adhere to the surface at 37°C in 5% CO$_2$; after 4 hr, the medium was replaced with Neurobasal medium supplemented with 2% B27, 0.5 mM glutamine, 15.6 μM glutamate, and 1% penicillin/streptomycin. Cells were grown for 4 d at 37°C in 5% CO$_2$ before lysis.

DRG neuron culture and transfection
Dissociated DRG neurons were isolated from adult female Wistar rats (3–5 months old) or from adult *MAP2*$^{-/-}$ or WT mice (3–5 months old) (gift of N. Hirokawa, University of Tokyo, Japan). The neurons were dissociated with collagenase type IV (Sigma) and 0.1% trypsin (Worthington) and centrifuged through a 15% BSA density gradient. Dissociated neurons were plated on coverslips coated with poly-D-lysine (20 μg/ml) and 1 μg/ml laminin (Sigma), and cultured in dissociated DRG culture medium (DMEM; Sigma), 1% FBS (Invitrogen), penicillin-streptomycin-fungizone (1 × ; Sigma) and kept at 37°C in 5% CO$_2$.

Dissociated DRG neurons in suspension were transfected using a Neon microporator (ThermoFisher), which electroporates within a micropipette tip. Approximately 1 × 10^5 cells were transfected per reaction, in a volume of 10 μl. Transfected cells were plated and cultured as described above, but without antibiotics for the first 24 hr after electroporation. Adherent dissociated DRG neurons were transfected using a cell culture plate electrode coupled to a NEPA electroporator (Nepagene) as instructed by the manufacturer.

COS7 and MRC5 cell culture and transfection
African Green Monkey SV40-transformed kidney fibroblast cells (COS7) and MRC5 cells were cultured in DMEM/Ham's F10 (50%/50%) supplemented with 10% FCS and 1% penicillin/streptomycin at 37°C and 5% CO2. Cells were seeded 24mm glass coverslips prior to transfection. MRC5 cells were transfected with or Fugene6 (Promega) and according to manufacturer's protocol. Coverslips with transfected cells were mounted in an imaging chamber and used for live-cell imaging.

METHOD DETAILS

DNA and shRNA constructs

The following mammalian expression plasmids have been described: pSuper vector,, GFP-MAP2C (LMW) (Kapitein et al., 2010), GFP-Rab6 (Schlager et al., 2014), TagRFP-Rab6 (Schlager et al., 2014), GFP-KIF5B-tail (dominant negative) (van Spronsen et al., 2013), HA-KIF5B-MDC(1-807)-FRB (Kapitein et al., 2010), KIF5B-MDC(1-807)-GFP-FRB (van Spronsen et. al., 2013), HA-KIF1C-MDC(1-397)-FRB (Kapitein et al., 2010), PEX-mRFP-FKBP (Kapitein et al., 2010), mCherry-Rab6-FKBP (Schlager et al., 2014), NPY-venus (Grigoriev et al., 2007), GFP-MT+Tip (Kapitein et al., 2010). All other constructs were created using PCR based strategies. Full length MAP2B was subcloned into GFP or TagRFP-expression vectors using the AgeI and SbfI restriction sites. The HA-KIF5B-MDC-FRB, the KIF5B-MDC-GFP-FRB and the mCherry-KIF5B truncations were generated by PCR using the full length human KIF5B as template (IMAGE clone 8991997) (van Spronsen et al., 2013). HA-KIF1A(657-1698) was generated using full-length rat KIF1A as a template (Accession XM_003750741), NPY-RFP construct was created by PCR using NPY-venus as a template. The following shRNAs were used in this study: MAP2-shRNA #1 and #2 (Kapitein et al., 2010); TRIM46-shRNA #1 and #2 (van Beuningen et al., 2015), KIF1A, KIF1B and C-shRNAs (Lipka et al., 2016). Neurofilament-L-shRNA (#1: UGGACAUUGAGAUUGCAGC, #2: GUCAA GAUGGCAUUGGACA and #3 CGCCUACUUAAGGCUAAGA). The complementary oligonucleotides were annealed and inserted into pSuper vector.

Preparation of tissue extracts and Immunoblotting

For tissue western blots, whole brains were dissected from adult wild-type or MAP2 KO mice and placed in ice-cold PBS, pH7.4. Samples were homogenized in homogenization buffer (150 mM NaCl, 50 mM Tris, 0.1% v/v SDS, 0.5% v/v NP-40, pH8, 1x complete protease inhibitors; Roche), briefly sonicated, centrifuged at 900 rpm, resuspended in 2x SDS sample buffer and boiled for 5 min. For cortical neuron western blots, cells were directly lysed in SDS-page sample buffer containing DTT, briefly sonicated, 10min boiled and subjected to Tris-Glycine SDS-page followed by blotting on nitrocellulose membranes.

Protein samples were separated by SDS-PAGE using 6%, 8% and 10% acrylamide gels, and transferred onto nitrocellulose membrane (Biorad). Protein transferred to the membrane was visualized by Ponceau-S staining and subsequently destained in PBS. Membranes were then incubated for 1 hr with agitation in blocking buffer (5% w/v skimmed milk, PBS). Incubation with primary antibody overnight at 4°C in blocking buffer containing 0.05% tween was followed by secondary antibody conjugated to horseradish peroxidase (Dako) incubation for 1 hr in 0.5% tween blocking buffer. Membranes were washed in PBS 0.05% tween after each antibody incubation. Blots were developed with enhanced chemiluminescent western blotting substrate.

GFP Immunoprecipitation

GFP-MAP2B fragments were cotransfected with mCherryKIF5B(370-560), mCherryKIF5B(560-807) or HA-KIF1A(657-1698) into HEK293T cells. One day after transfection, cells were lysed in a buffer containing 20 mM Tris-HCl, pH 7.5, 150 mM NaCl, 1% Triton X-100, and protease inhibitors (Complete; Roche) and purified with GFP-Trap magnetic beads (Chromotek) according to the manufacturer's instructions. The proteins retained on the beads were analyzed by SDS-PAGE and western blotting.

Microtubule binding assay in fixed COS7 cells

COS7 cells were plated on glass coverslips and transfected with plasmids encoding the proteins of interest. One day later, the cells were incubated in Ringer's buffer (10 mM HEPES, 155 mM NaCl, 5 mM KCl, 2 mM CaCl$_2$, 1 mM MgCl$_2$, 2 mM NaH$_2$PO$_4$, 10 mM glucose, pH 7.2) for 5 min at 37°C. Cells were treated with 0.1 μg/ml SLO in Ringer's buffer + 10 mg/ml BSA for 30 s. After washing three times with Buffer I (25 mM HEPES, 5 mM MgCl$_2$, 115 mM KOAc, 5 mM NaOAc, 0.5 mM EGTA, 10 mg/ml BSA, pH 7.2) cells were incubated with Ringer's buffer containing 1 mM AMPPNP for 5 min. Cells were fixed and imaged on a laser scanning confocal microscope.

Hippocampal and DRG Neuron Immunofluorescence

Neurons on glass coverslips were fixed for 10 min in 4% paraformaldehyde at room temperature then labeled with primary antibodies in PBS and 10% goat serum for 1 hr and secondary antibodies in PBS for 1 hr. PBS washes were performed after each antibody incubation. Coverslips were mounted on glass slides in Fluorsave (Calbiochem). To visualize EB3 comets, dissociated neurons were fixed in ice-cold methanol for 5 min followed by 4% PFA for 20 min. Images were captured using an upright Nikon Eclipse 80i microscope with 20x 0.75 N.A. Plan Fluor objective, 40x 1.3 N.A. Plan Fluor objective, 60x 1.4 N.A Plan Apo VC objective and a Photometrics CoolSNAP HQ2 CCD camera, using the Nikon NIS Br software. All images were scaled and prepared in ImageJ and Adobe IllustratorCS.

Whole DRG Immunohistochemistry

Whole DRGs were obtained from 4% paraformaldehyde perfused adult Wistar rats. The DRGs were cryoprotected by overnight incubation in 30% sucrose, sectioned at 40 μm on a freezing microtome. Sections where either heated in a microwave for antigen retrieval for 10 min in Sodium Citrate buffer (5mM, pH 6). Sections were blocked for 1 hr using 10% normal goat serum in 0.2% Triton X-100 PBS for 1 hr followed by primary and secondary antibody incubation (in 10% normal goat serum in 0.2% Triton X-100 PBS) prior to mounting in Vectashield mounting medium (Vectorlabs).

Epifluorescence microscopy

Fluorescent microscopy was performed using a Nikon Eclipse 80i with Plan Apo VC 100x numerical aperture (NA) 1.40 oil, Plan Apo VC 60x NA 1.40 oil, Plan Fluor 40x NA 1.30 oil, and a Plan Fluor 20x NA 0.75 objective (Nikon), equipped with a CoolSNAP HQ2 CCD camera (Roper Scientific).

Confocal microscopy

Confocal laser scanning confocal microscopy was performed using a LSM-700 system (Zeiss) with a Plan-Apochromat 63x NA 1.40 oil DIC, EC Plan-Neofluar 40x NA1.30 Oil DIC, and a Plan-Apochromat 20x NA 0.8 objective.

Laser Scanning Confocal and STED microscopy

Confocal and gated STED imaging for Figure S7A,B was performed with Leica TCS SP8 STED 3X microscope using HC PL APO 100x/1.4 oil STED WHITE objective. Secondary antibody with Alexa 488 was used to label tubulin and during imaging it was excited with the 488 nm wavelength of pulsed white laser (80MHz) and depleted with CW 592 nm STED laser. Secondary Alexa 647 antibody labeled MAP2 and was imaged with 633 nm of white laser and depleted with 775 nm pulsed lased. Images were acquired in 2D STED mode with vortex phase mask. Depletion laser power was equal to 50% of maximum power and we used an internal Leica GaAsP HyD hybrid detector with a time gate of $1 \leq t_g \leq 8$ ns. Confocal imaging of MAP2 stained with Alexa 647 and Rab6 with Alexa 568 secondary antibodies was performed on the same setup using white laser and standard excitation and emission settings from LAS X controlling software library.

Live-cell imaging
Spinning disk confocal

Live-cell imaging of DRG neurons or MRC5 cells was performed on an inverted research spinning-disk microscope Nikon Eclipse Ti-E (Nikon) with perfect focus system (Nikon), equipped with Nikon CFI Apo TIRF 100 × 1.49 NA oil objective (Nikon), Plan Apo VC 60x N.A. 1.40 oil objective (Nikon), Plan Fluor 40x N.A. 1.30 oil objective (Nikon), CSU-X1-A1 motorized spinning disc (Yokogawa), Photometrics Evolve 512 EMCCD (Roper Scientific), and controlled with MetaMorph 7.7 software (Molecular Devices). 491 nm (100 mW) Calypso (Cobolt) and 561nm (100 mW) Jive (Cobolt) lasers were used for excitation. The spinning disc was equipped with 405-491-561 tipple band mirror and ET-GFP, ET-mCherry, and ET-GFP/mCherry emission filters (Chroma). For simultaneous imaging of green and red fluorescence we used DualView dual-channel beamsplitter (DV2, Roper Scientific) equipped with dichroic filter 565dcxr (Chroma) and ET-GFP and ET-mCherry emission filters (Chroma). The microscope's magnified image was projected onto the chip of the 16-bit camera with intermediate lens 2.0 × (Edmund Optics) with a final magnification of 0.066 mkm/pixel. To keep cells at 37°C, we used stage top incubator (model INUBG2E-ZILCS; Tokai Hit). Rapalog1 (AP21967) was dissolved to 1 mM in ethanol. For induction of motility during image acquisition, 0.2 mL of culture medium with rapalog1 (4 μM) was added to establish a final rapalog1 concentration of 1 mM (Kapitein et al., 2010).

Total internal reflection fluorescence microscopy

Live-imaging of MRC5 cells or COS7 cells was carried out using total internal reflection fluorescence microscopy (TIRFM). TIRFM was performed on an inverted microscope (Nikon Eclipse Ti-E; Nikon) with Perfect Focus System (Nikon) with Nikon CFI Apo TIRF 100x NA 1.49 oil objective (Nikon), equipped with an Evolve 512 EMCCD camera (Roper Scientific), and a CoolSNAP HQ2 CCD camera (Roper Scientific), and controlled with MetaMorph 7.7.5 software (Molecular Devices). To keep the samples at 37°C (cells), we used stage top incubator model INUBG2EZILCS (Tokai Hit). The microscope was equipped with TIRF-E motorized TIRF illuminator modified by Roper Scientific/PICTIBiSA (Institut Curie). For regular imaging, we used 491-nm, 100-mW Calypso (Cobolt) and 561-nm, 100-mW Jive (Cobolt) lasers for excitation. We used ET-GFP filter set (Chroma) for imaging of proteins tagged with GFP; ET-mCherry filter set (Chroma) for imaging of proteins tagged with mCherry, TagRFP or RFP. For simultaneous imaging of green and red fluorescence, we used Evolve 512 camera, triple-band TIRF polychroic ZT405/488/561rpc (Chroma), and triple-band laser emission filter ZET405/488/561 m (Chroma), mounted in the metal cube (Chroma; 91032) together with Optosplit III beamsplitter (Cairn Research, UK) equipped with double-emission filter cube configured with ET525/50 m, ET630/75 m, and T585LPXR (Chroma). Microscope was equipped with an ILas system (Roper Scientific France/PICT-IBiSA) for FRAP and photoablation. For FRAP experiments we used 491-nm laser described above with 100% power. The images were projected onto the chip of Evolve 512 camera with the intermediate lens 2.5 × (Nikon C mount adaptor 2.5 ×) or onto the chip of the CoolSNAP HQ2 without an additional lens. In both cases, the final magnification was 0.063 μm per pixel.

Image analysis and quantification
Quantification of immunofluorescence

All images were taken at the same settings for light and exposure with parameters adjusted so that the pixel intensities were below saturation. Images were analyzed by Fiji analysis software and Metamorph (Molecular Devices). For quantification of fluorescence intensity levels and distribution in the proximal region of the axon, the length of an axon was traced using as starting point the border of the cell body and the nascent axon. For quantification of fluorescence intensity levels in the cell bodies, the cell body area was traced. The intensity of the background was similarly measured in areas adjacent to the axons or cell bodies and subtracted giving a final intensity value per axon or cell body. Ratios of cell body versus growth cone TagRFP-Rab6

intensities were determined by measuring the integrated mean gray value using Fiji. Ratios were averaged over multiple neurons and experiments.

Quantification of axonal length

ImageJ software was used to analyze the images. The drawing tool was used to trace and measure the length of the longest neurite per neuron from the axon hillock to the growth cone.

Quantification of neurite number

ImageJ software was used to analyze the images of control or MAP2 knockdown DRG neurons that had either been stained for Tubulin-β-III or transfected with a plasmid encoding GFP. The number of neurites per cell body was scored manually after visual inspection.

Analysis of vesicle transport after photobleaching in the proximal axon of DRG neurons

The proximal segments of DRG axons were photobleached using an ILas system (Roper Scientific France/PICT-IBiSA, Institute Curie). Briefly, an area of 20 μm located 1-2 μm away from the cell body was photobleached. Movies were subsequently acquired using spinning disk confocal microscopy (100x objective) with stream acquisition of 10 fps for 2 min. Acquisitions were analyzed using Fiji. Kymographs were created using a segmented line along the axon from the soma toward the axon tip. On the kymographs single vesicle movement episodes were distinguished as tilted straight lines. The number of vesicles moving beyond 1 μm from either side of the photobleached area was quantified as anterograde or retrograde moving vesicles.

Analysis of vesicle transport along whole DRG axons

The same axon was imaged from the cell body border to the growth cone using spinning disk confocal microscopy (using 60x objective) with a stream acquisition of 10 fps for 2 min. Acquisitions were analyzed using Fiji. Kymographs were created using a segmented line along the axon from the soma toward the axon tip. On the kymographs single vesicle movement episodes were distinguished as tilted straight lines. The length and the duration of each growth episode were measured as horizontal and vertical projections of those lines, respectively. The movement velocity was calculated as a ratio of those values. The length of each growth episode corresponded to the run length. Single vesicle pauses were distinguished as straight lines. The duration of each pausing episode was measured and averaged per kymograph.

Analysis of GFP-MT+TIP comets in proximal DRG axons

The axon was imaged using spinning disk confocal microscopy (using 100x objective) with an acquisition of 5 fps for 1 min. Movies of axons labeled with GFP-MT+TIP were imported into Fiji software. Maximum intensity projections of those movies contained easily visible tracks corresponding to the microtubules growth episodes marked by GFP-MT+TIP comets. Kymographs were built along those curves. On the kymographs, single growth episodes were distinguished as bright tilted straight lines. The length and the duration of each growth episode were measured as horizontal and vertical projections of those lines, respectively. The growth velocity was calculated as a ratio of those values.

Analysis of the decomposition of anterograde Rab6 velocities in DRG axons

Fitting of velocities' distribution was performed using GraphPad Prism 5.02 for Windows (GraphPad Software, San Diego, CA). First, the normalized histogram of velocities was built with the bin size of 0.3 μm/s. It was used for simultaneous fitting with one Gaussian function and with a sum of two Gaussians using equations:

$$P_{one}(v) = A \exp\left(-\frac{(v-\overline{v})^2}{2\sigma^2}\right),$$

$$P_{two}(v) = A_{slow} \exp\left(-\frac{(v-\overline{v}_{slow})^2}{2\sigma_{slow}^2}\right) + A_{fast} \exp\left(-\frac{(v-\overline{v}_{fast})^2}{2\sigma_{fast}^2}\right)$$

where $\overline{v}, \overline{v}_{slow}, \overline{v}_{fast}$ are mean velocity values, $\sigma, \sigma_{slow}, \sigma_{fast}$ are standard deviations and A, A_{slow}, A_{fast} are corresponding amplitudes. The best fit out of two was chosen using extra sum-of-squares F test with the P value of 0.05. In case of a sum of two Gaussians fit the calculation of corresponding slow f_{slow} and fast f_{fast} fractions was based on area under curve, according to:

$$AUC_{slow} = A_{slow}\sigma_{slow}\sqrt{2\pi}, \ AUC_{fast} = A_{fast}\sigma_{fast}\sqrt{2\pi}, \ AUC_{total} = AUC_{slow} + AUC_{fast},$$

$$f_{slow} = \frac{AUC_{slow}}{AUC_{total}}, \ f_{fast} = \frac{AUC_{fast}}{AUC_{total}}.$$

The error in the determination of fraction was calculated according to the propagation of uncertainties (Taylor, 1997) using fit errors for each parameter.

Analysis of KIF5-GFP single molecule motility in DRG axons

DRG proximal axons were imaged using spinning disk confocal microscopy (using 100x objective) with a stream acquisition of 30 fps for 60 s. Acquisitions were analyzed using Fiji. Kymographs were created using a segmented line along the axon from the soma toward the axon tip. On the kymographs single vesicle movement episodes were distinguished as titled straight lines. The length and the duration of each growth episode were measured as horizontal and vertical projections of those lines, respectively. The movement velocity was calculated as a ratio of those values.

Analysis of Rab6 or peroxisome velocities in MRC5 cells

MRC5 cells were imaged using spinning disk microscopy (using 100x objective) with a stream acquisition of 10 fps for 50 s. Analysis of velocities was performed manually using kymograph assay, by computing the mean value for each cell and then averaging the values for cells within a certain category; n for each measurement corresponds to the number of velocity events counted in the indicated number of cells over 2-3 independent experiments.

Analysis of FRAP experiments

To characterize temporal dynamics of protein-GFP fusion turnover, a round region of 5 μm in diameter within COS7 cells was bleached with high laser power and fluorescence recovery was observed. The mean intensity of this region was corrected by subtracting at each frame the mean intensity of a background region next to it $I(t) = I_{bleachedregion}(t) - I_{background}(t)$. The normalization of recovery $R_{norm}(t)$ was calculated according to the formula:

$$R_{norm}(t) = \frac{I(t) - I(0)}{\langle I(\Delta t) \rangle - I(0)}$$

where $I(0)$ corresponds to the region's mean intensity directly after bleaching, $\langle I(\Delta t) \rangle$ –intensity averaged over 5 initial frames before bleaching. To account for the bleaching due to imaging itself, additional correction was performed using intensity of a non-bleached region within the cell:

$$R(t) = R_{norm}(t) \frac{\langle I_{control}(\Delta t) - I_{background}(\Delta t) \rangle}{I_{control}(t) - I_{background}(t)}$$

where $I_{control}$ corresponds to the mean intensity of the non-bleached region and time interval Δt denotes 5 initial frames before bleaching.

The recovery curves of multiple cells were pooled together and averaged and the characteristic time of recovery τ and maximum recovery fraction R_{max} was obtained by fitting the following equation in GraphPad Prism:

$$R(t) = R_{max}(1 - \exp(-t/\tau))$$

Mathematical model describing the spreading of vesicles in the axon

To describe the flow of moving vesicles in axons we assumed their constant appearance from the cell body, located at the origin of coordinates. The vesicles move anterogradely with average speed V and can dock or go through exocytosis with a constant rate k_{ex}. Assuming a "semi-infinite" geometry of the axon, the number (or density) of moving vesicles $N(x,t)$ along the axon is described by the kinetic equation:

$$\frac{\partial N(x,t)}{\partial t} = -k_{ex}N - V\frac{\partial N}{\partial x} \tag{1}$$

where the first term accounts for exocytosis and the second term describes the movement of vesicles.

Solving the equation for the steady state, when the rate of change is equal to zero gives:

$$N(x) = N_0 \exp\left(-\frac{k_{ex}}{V}x\right) \tag{2}$$

where N_0 is equal to the number of vesicles leaving cell body. Equation (2) was fitted to the experimental data with addition of an offset responsible for the remaining MAP2-independent transport. The mean speed values for control and MAP2 knockdown conditions were constant and were taken from the experimental data (Figure 5D) by averaging values along the axon length. For the control condition the fitting parameters were N_0 and k_{ex}. Fitting provided corresponding parameters values of 36.2 and $2.8 \cdot 10^{-3}$ s^{-1}, respectively. For the MAP2 knockdown condition we scaled the value of vesicles leaving cell body N_0 for the same factor as observed in experiments (Figure 3F) and kept the values of k_{ex} and offset the same. The final predicted curve is shown in red in Figure 5C.

QUANTIFICATION AND STATISTICAL ANALYSIS

Statistical parameters including the definitions and exact values of n (e.g., number of experiments, number of cells, etc), distributions and deviations are reported in Table S1, Figures and corresponding Figure Legends. All data was collected and analyzed from at least 3 independent experiments. Data and statistical analysis were performed with GraphPad software. Statistical analysis includes unpaired Students's t test (two tailed), Mann-Whitney U test (two tailed) (not significant is p > 0.05, *p < 0.05, **p < 0.01, ***p < 0.001). Diagrams were made using GraphPad Prism software.